



**Combined, time-resolved, in situ neutron reflectometry and x-ray diffraction analysis of dynamic SEI formation during electrochemical N<sub>2</sub> reduction**

Journal:	<i>Energy &amp; Environmental Science</i>
Manuscript ID	EE-ART-11-2022-003694.R2
Article Type:	Paper
Date Submitted by the Author:	10-May-2023
Complete List of Authors:	<p>Blair, Sarah; Stanford University, Chemical Engineering, 443 Via Ortega; SLAC National Accelerator Laboratory, SUNCAT Center for Interface Science and Catalysis, 2575 Sand Hill Rd</p> <p>Doucet, Mathieu; Oak Ridge National Laboratory, Neutron Scattering Division, 1 Bethel Valley Rd</p> <p>Niemann, Valerie; Stanford University, Chemical Engineering, 443 Via Ortega; SLAC National Accelerator Laboratory, SUNCAT Center for Interface Science and Catalysis, 2575 Sand Hill Rd</p> <p>Stone, Kevin; SLAC National Accelerator Laboratory, SSRL</p> <p>Kreider, Melissa; Stanford University, Chemical Engineering; SLAC National Accelerator Laboratory, SUNCAT Center for Interface Science and Catalysis, 2575 Sand Hill Rd</p> <p>Browning, Jim; Oak Ridge National Laboratory, Neutron Scattering Division, 1 Bethel Valley Rd</p> <p>Halbert, Candice; Oak Ridge National Laboratory, Neutron Scattering Division, 1 Bethel Valley Rd</p> <p>Wang, Hanyu; Oak Ridge National Laboratory, Center for Nanophase Materials Sciences</p> <p>Benedek, Peter; Stanford University, Chemical Engineering, 443 Via Ortega; SLAC National Accelerator Laboratory, SUNCAT Center for Interface Science and Catalysis, 2575 Sand Hill Rd</p> <p>McShane, Eric; Stanford University, Chemical Engineering, 443 Via Ortega</p> <p>Nielander, Adam; SLAC National Accelerator Laboratory, SUNCAT Center for Interface Science and Catalysis, 2575 Sand Hill Rd</p> <p>Gallo, Alessandro; SLAC National Accelerator Laboratory, SUNCAT Center for Interface Science and Catalysis, 2575 Sand Hill Rd</p> <p>Jaramillo, Thomas; Stanford University, Associate Professor of Chemical Engineering, 443 Via Ortega, Rm 305; SLAC National Accelerator Laboratory, SUNCAT Center for Interface Science and Catalysis, 2575 Sand Hill Rd</p>

SCHOLARONE™  
Manuscripts

Ammonia is produced on a massive scale ( $> 170 \text{ Mton yr}^{-1}$ ) and is both a critical source of fertilizer for global agriculture and a source of large-scale global  $\text{CO}_2$  emissions ( $420 \text{ Mton yr}^{-1}$ ). The electrochemical reduction of  $\text{N}_2$  to  $\text{NH}_3$  (NRR) has been proposed as an alternative path toward sustainable, decentralizable  $\text{NH}_3$ , with significant effort being directed toward non-aqueous, Li-mediated NRR (Li-NRR). This system has been shown to reliably produce ammonia and can be promoted by cycling the current driving the reaction between open-circuit conditions and periods of applied current density. Herein, we have investigated the dynamics of layer formation at the electrode-electrolyte interface during current cycling under Li-NRR conditions using *in situ* time-resolved neutron reflectometry and grazing-incidence synchrotron X-ray diffraction. These observations of the solid-electrolyte interphase (SEI) and Li-containing layers at the interface suggest that benefits associated with current cycling is related to the mobility of Li-containing species within a thin layer at the cathode surface and the dissolution and subsequent reformation of the SEI layer during current cycling. This combination of techniques thus provides unique insight into the SEI layer of this system, which has been shown to be key to performance improvements.

## ARTICLE

## Combined, time-resolved, *in situ* neutron reflectometry and x-ray diffraction analysis of dynamic SEI formation during electrochemical N<sub>2</sub> reduction

Received 00th January 20xx,  
Accepted 00th January 20xx

DOI: 10.1039/x0xx00000x

Sarah J. Blair<sup>†a,c</sup>, Mathieu Doucet<sup>\*†b</sup>, Valerie A. Niemann<sup>a,c</sup>, Kevin H. Stone<sup>d</sup>, Melissa E. Kreider<sup>a,c</sup>, James F. Browning<sup>b</sup>, Candice E. Halbert<sup>b</sup>, Hanyu Wang<sup>e</sup>, Peter Benedek<sup>a,c</sup>, Eric J. McShane<sup>a</sup>, Adam C. Nielander<sup>\*c</sup>, Alessandro Gallo<sup>\*c</sup>, Thomas F. Jaramillo<sup>\*a,c</sup>

One means of improving performance for electrochemical ammonia production through the Li-mediated N<sub>2</sub> reduction reaction (Li-NRR) is by cycling the current driving the reaction between open-circuit conditions and periods of applied current density. Herein, we have investigated the dynamics of the electrode-electrolyte interface under Li-NRR conditions during current cycling using *in situ* time-resolved neutron reflectometry and grazing-incidence synchrotron X-ray diffraction. During cycling, measured neutron reflectivity curves indicated bilayer formation in which Li-containing species such as LiOH, Li<sub>2</sub>O, and small quantities of Li<sub>3</sub>N and metallic Li primarily appeared in a thin layer at the cathode surface, above which formed a much larger, porous, 'solid-electrolyte interface' (SEI) layer. Upon return to open-circuit conditions, Li-containing species quickly moved out of the thin layer, leaving a compact, stable layer of decomposition products underneath the SEI layer. This SEI layer concomitantly filled with electrolyte or dissolved, becoming indistinguishable from the electrolyte via contrast in scattering-length density (SLD). During the second current cycle, Li-containing species again preferentially deposited directly atop the cathode, with the thick SEI-like layer again appearing within a minute. This SEI layer exhibited a lower SLD more quickly than in the first cycle, which might suggest that Li-containing species become distributed within the porous SEI layer. Thus, these time-resolved observations of SEI and plated layers during current cycling suggest that benefits associated with return to open-circuit conditions between periods of applied current density may be related to the concomitant loss of Li-containing species from a thin layer at the cathode surface into a porous SEI layer that becomes filled with electrolyte or dissolves.

<sup>a</sup> Department of Chemical Engineering, Stanford University, Stanford, CA 94305, United States.

<sup>b</sup> Neutron Scattering Division, Oak Ridge National Laboratory, Oak Ridge, TN 37831, United States.

<sup>c</sup> SUNCAT Center for Interface Science and Catalysis, SLAC National Accelerator Laboratory, 2575 Sand Hill Road, Menlo Park, CA 94025, United States.

<sup>d</sup> Stanford Synchrotron Radiation Lightsource, SLAC National Accelerator Laboratory, 2575 Sand Hill Road, Menlo Park, CA 94025, United States.

<sup>e</sup> Center for Nanophase Materials Sciences, Oak Ridge National Laboratory, Oak Ridge, TN 37831, United States.

† These authors contributed equally to this work.

\*Corresponding author.

Electronic Supplementary Information (ESI) available: [Detailed experimental methods; photos of experimental setup; chronopotentiometry for all cycles; reflectivity data, model curves, and SLD profiles for steady-state measurements along with model parameters; table of calculated SLD values for relevant interfacial species; XPS depth profile of representative cathode sample before electrochemistry; benchtop chronopotentiometric cycling experiments with NH<sub>3</sub> quantification; time-resolved reflectivity data and model curves for Cycle 1; table of model parameters corresponding to model reflectivity curves for Cycle 1 reflectivity data; linear-sweep voltammetry in electrochemical cell; time-resolved reflectivity data and model curves for OCP following Cycle 1; time-resolved SLD profiles for select model curves at OCP; table of model parameters corresponding to models of time-resolved reflectivity data at OCP; time-resolved reflectivity data and model curves for Cycle 2; table of model parameters corresponding to model reflectivity curves for Cycle 2 reflectivity data; potential versus time for additional cycles of chronopotentiometry and open-circuit conditions.<sup>31,55–62</sup>]. See DOI: 10.1039/x0xx00000x

## Introduction

Ammonia is produced on a massive scale (> 170 Mton yr<sup>-1</sup>) and is a critical fertilizer source to support global agriculture.<sup>1,2</sup> Interest in the use of ammonia as a renewable energy carrier has additionally emerged in recent years both as a hydrogen storage vector and as a fuel.<sup>3–6</sup> Currently, ammonia is produced directly from N<sub>2</sub> and H<sub>2</sub> industrially via the Haber-Bosch process, which operates at high temperatures (450–500 °C) and pressures (200 bar), is driven by fossil fuel sources, and produces significant CO<sub>2</sub> emissions (420 Mton yr<sup>-1</sup>).<sup>4</sup>

The electrochemical N<sub>2</sub> reduction reaction (NRR) to NH<sub>3</sub> has been proposed as a path toward sustainable, decentralizable NH<sub>3</sub> production — it can be directly coupled to renewable electricity, and it can operate at low temperatures and pressures. In particular, significant effort has been directed toward non-aqueous, Li-mediated NRR (Li-NRR), which has been shown to reliably produce ammonia via a posited mechanism in which Li is first deposited onto the cathode and subsequently reacts with N<sub>2</sub> and EtOH in the non-aqueous electrolyte to produce NH<sub>3</sub> and Li ethoxide, with parasitic reactions also occurring between deposited Li and the electrolyte that lead to losses in activity toward the Li-NRR.<sup>7,8,9</sup> A variety of methods have been explored to improve Li-NRR performance,<sup>10–15</sup> and cycling the applied current between open-circuit and cathodic conditions at potentials negative of E<sub>Li+/Li</sub> has been shown to improve selectivity, increasing FE<sub>NH<sub>3</sub></sub> by 75% relative to constant-current conditions.<sup>16</sup> This improvement in selectivity has been attributed to a variety of factors, including 1) the limiting of total Li deposited at the electrode surface, promoting a smoother surface that facilitates Li<sub>3</sub>N formation, 2) the formation of passivating solid-electrolyte interphase (SEI) species that maintain electrode stability and control proton, Li, and N<sub>2</sub> transport to the electrode, and 3) the prevention of solvent decomposition at the cathode surface.<sup>16–18</sup>

However, understanding the relationship between the electrode-electrolyte interface structure and electrochemical performance is hampered by the highly reactive nature and air/water sensitivity of these non-aqueous and Li-containing system components. This makes it difficult to accurately observe the nature of the interface as it is under operating conditions using *ex situ* techniques and highlights the need for *in situ* techniques to interrogate the interfacial structure relevant to the electrochemical reaction.<sup>19–21</sup> Neutron techniques are particularly well-suited to the study of Li species because, unlike X-ray scattering cross sections, neutron scattering cross-sections are not directly related to elemental atomic number. Further, reflectivity methods can provide indicators of composition, thickness, and roughness of both amorphous and crystalline material layers.<sup>22–28</sup> These methods are particularly powerful when coupled with the ability to identify crystalline material phases provided by *in situ* grazing-incidence X-ray diffraction (GI-XRD). Thus, the combination of neutron

reflectometry and GI-XRD is uniquely well-suited to the mechanistic study of non-aqueous, Li-NRR because it affords the ability to provide information concerning amorphous SEI layer composition with an increased sensitivity to Li species along with crystalline material phases formed at the electrode surface.

We have previously used time-resolved neutron reflectometry to investigate Li-NRR at -0.1 mA cm<sup>-2</sup> under constant current conditions, finding that at short times (~5 min), Li-rich surface layers form at the electrode surface.<sup>29</sup> Herein, we have extended the use of *in situ* time-resolved neutron reflectometry to investigate the electrode-electrolyte interface during current cycling under Li-NRR conditions and at higher current densities (-0.5 mA cm<sup>-2</sup>). We have combined this technique with *in situ* synchrotron grazing-incidence X-ray diffraction (GI-XRD) to evaluate the resulting layer composition and formation dynamics in order to gain a deeper understanding of the complex electrode/electrolyte interfacial dynamics that influence Li-NRR performance under current cycling conditions.

## Experimental

Experimental details can be found in the Supporting Information. Briefly, electrochemical measurements were made using a previously reported electrochemical cell designed specifically for neutron reflectivity measurements.<sup>30</sup> The cathode consisted of 50 nm of Mo deposited via physical vapor deposition (PVD) onto a Si wafer (Figure S1). The anode consisted of 100 nm Pt on a 3-nm Ti sticking layer deposited via PVD onto a Si wafer. The electrolyte consisted of d<sub>8</sub>-THF, 0.2 M LiClO<sub>4</sub>, and 0.17 M EtOH and was saturated with purified N<sub>2</sub>. Care was taken to ensure that the system was closed to avoid inhalation of the THF-based electrolyte. All electrochemical cells were prepared in an Ar glovebox prior to testing (Figure S2).

Neutron reflectivity measurements were performed using the Liquids Reflectometer (LR) at the Spallation Neutron Source at Oak Ridge National Laboratory. The LR is a time-of-flight (TOF) reflectometer with a wavelength band of approximately 3.5 Å provided by an accelerator pulse frequency of 60 Hz. It is capable of continuous single neutron detection, such that data acquired over a long period of time can be split into time intervals as needed. Two types of neutron reflectivity measurements were performed in this work, one of which we have defined as a “steady-state” measurement, and one of which we have designated a “time-resolved” measurement. The steady-state measurement utilizes a wide wavevector transfer range (0.008 < Q < 0.2 1/Å), defined by  $Q = 4\pi \sin(\theta)/\lambda$ , where  $\theta$  is the incident angle of the neutron and  $\lambda$  its wavelength. This measurement employs seven configurations that are defined by a particular value of  $\theta$  and wavelength band. For the time-resolved configuration, a smaller Q-range was used by selecting a single configuration defined by a  $\theta$ -value and wavelength band such that scattered neutrons were counted continuously and the

reflectivity data later binned into specific time intervals. The binning time interval was chosen by examining various time intervals and determining the largest time interval during which the reflectivity measurements of the interface were approximately constant within counting statistics. This allowed for usage of the maximum number of neutron counts for each time interval in order to facilitate modeling of the reflectivity curves while still allowing us to distinguish changes occurring at the electrode-electrolyte interface. The time intervals employed in this work ranged from 15 seconds to 30 seconds.

The neutron reflectivity measurements were then modeled using the *refl1d* package,<sup>31</sup> which uses a set of slabs, each with a thickness, scattering-length density (SLD), and roughness parameter, to fit the reflectivity curves. The SLD is related to the neutron scattering length and volumetric density of the atoms in each layer and is defined by  $SLD(z) = \sum_i n_i b_i$  where  $b_i$  is the coherent scattering length and  $n_i$  is the number density of nuclei of type  $i$  as a function of depth  $z$ . The extracted SLD profile provides information about the composition of thin films as a function of depth.

Synchrotron GI-XRD measurements with an incident X-ray energy of 17 keV (0.729 Å) were performed *in situ* at beam line 2-1 at the Stanford Synchrotron Radiation Lightsource (SSRL) using a custom-designed electrochemical cell.<sup>32</sup> Measurements were executed at an incident X-ray angle of 0.2 – 0.5°, with the grazing incidence angle and Pilatus 100K area detector controlled using a Huber two-circle goniometer. A  $2\theta$  window of 9° - 30° was used in order to capture the peaks of interest of Li-containing species, which are concentrated at  $2\theta < 20^\circ$ , and measurements were taken using 60 points within this wavelength range, at 3 sec/point. Two-dimensional Pilatus images were acquired, and these images were then converted into  $2\theta$ -values by performing an integration across the image pixels. A spline interpolation method was then used to fit the baseline of these integrated data, and this baseline was subtracted to correct for the measurement background. To compare between measurements, the background-subtracted data were then normalized to the maximum intensity value located between  $2\theta = 18^\circ$  and  $2\theta = 19^\circ$  which corresponded to the Mo peak at  $\sim 2\theta = 18.5^\circ$ . All post-experimental cathode samples were placed into an excess of mineral oil to avoid exposure of any plated lithium metal to air or water.

## Results & discussion

### Initial state of the electrode-electrolyte interface

A neutron reflectivity measurement of the cathode-electrolyte interface in the filled electrochemical cell was executed at open-circuit conditions using the steady-state measurement configuration to establish a baseline for subsequent measurements and models. We describe this initial measurement as “OCP 1” (Figure S3; OCP = open-circuit potential). Figure 1 shows

chronopotentiometry (Figure 1a), reflectivity data (Figure 1b), and corresponding reflectivity models and SLD profiles (Figure 1c). Initial steady-state measurements at OCP are presented in Figures 1b and 1c. The model of this reflectivity curve at OCP (Figures 1b and S4) corresponds to the SLD profile shown on Figure 1c (“Pre cycle 1”), providing a description of the electrode-electrolyte interface in its initial state. The “Pre cycle 1” model shows a layer directly atop the Si wafer with a thickness of 500 Å and SLD of  $4.35 \times 10^{-6} \text{ \AA}^{-2}$  (Table S1), which is consistent with the deposited Mo layer (Table S2). A layer, which we identify as Layer 1, with thickness 49 Å and slightly lower SLD value ( $4.2 \times 10^{-6} \text{ \AA}^{-2}$ ) was required on top of the Mo layer to achieve a satisfactory model of the data. We have attributed this surface layer to an oxidized Mo layer (see Figure S4), which would be expected to form on a Mo surface upon exposure to air and is further supported by x-ray photoelectron spectroscopy (XPS) analysis (Figure S5).<sup>33</sup> Above the oxide layer, the model shows an increase in SLD value to  $6.2 \times 10^{-6} \text{ \AA}^{-2}$ , which is consistent with the expected SLD value of the  $d_8$ -THF-based electrolyte (Table S2).

### Overview of the dynamics of the electrode-electrolyte interface

Table 1 presents an overview of the results that will be referred to throughout this work, with Row 1 corresponding to measurements of the initial state of electrode-electrolyte interface, as described above. For the measurements of the dynamic electrode-electrolyte interface detailed below, in brief, we observed two distinct layers, noted Layer 1 and Layer 2; Layer 2 was ascribed to an SEI layer atop a thinner layer (Layer 1) in which lithium-containing species were concentrated. The SEI layer (Layer 2) was observed to appear and disappear throughout the measurements based on the experimental conditions, with the thickness and composition of each layer being a strong function of the applied current. In particular, lithium-containing species were found to be mobile into and out of Layer 1 depending on whether the electrode was under open-circuit conditions or an applied current.

### Time-resolved measurements of the first application of current density

After having established open circuit conditions (Row 1), we then applied a current density of  $-0.5 \text{ mA cm}^{-2}$  to the cathode for 2 min; Rows 2-5 of Table 1 note observations in 15-second intervals for the first minute. A geometric current density of  $-0.5 \text{ mA cm}^{-2}$  was chosen because this value is close to the geometric current densities of  $-1$  to  $-2 \text{ mA cm}^{-2}$  that are often reported for other planar Li-NRR systems while remaining low enough to maintain a sufficiently smooth, thin sample surface to obtain well-defined reflectivity curves that could be modeled (see SI). We performed  $\text{NH}_3$  quantification in benchtop cycling experiments under similar conditions in the same electrochemical cell (Figure S6). These experiments showed efficacy toward producing  $\text{NH}_3$ , though Faradaic efficiencies are low as would be expected for a low-volume cell through which  $\text{N}_2$  is not continuously sparged nor electrolyte circulated. We posit that the initial conditions at the electrolyte/electrode interface are sufficiently reflective of the

conditions in cells designed for higher performance Li-NRR such that the knowledge gained from the interface formed herein can be broadly instructive toward understanding interfacial layer development during Li-NRR. We thus focus our discussion on Li

**Table 1.** Overview of dynamic neutron reflectivity results

Row	Electrochemistry	Time interval	Layer 1	Layer 2	Interpretation
1	Initial open-circuit conditions, measured in "steady-state" configuration	~1 hour for measurement, (Figure 1c, Pre cycle 1)	Layer with SLD slightly lower than Mo metal	N/A	MoO <sub>x</sub> layer atop Mo metal cathode
2	1 <sup>st</sup> CP (-0.5 mA cm <sup>-2</sup> )	0 < t < 15 s (Figure 1c, blue)	SLD decreases with little change in thickness	N/A	Concomitant increase in lithium content and reduction of surface MoO <sub>x</sub>
3		15 < t < 30 s (Figure 1c, yellow)	SLD decreases; thickness increases	N/A	Continued increase of lithium-containing species in Layer 1
4		30 < t < 45 s (Figure 1c, light green)	SLD decreases slightly	Thick layer with higher SLD	An SEI layer likely consisting of electrolyte decomposition products appears atop Layer 1
5		45 < t < 60 s (Figure 1c, red)	SLD decreases significantly and layer becomes thicker/more diffuse	SLD and thickness decrease	Content of lithium-containing species in Layer 1 increases significantly, causing layer thickness to increase quickly and become more diffuse with SEI layer (Layer 2)
6		Open circuit, where t = 0 s corresponds to 7 min following the return to OCP	0 < t < 30 s (Figure 3c, blue)	SLD increases	SLD remains at same value with larger thickness
7	870 < t < 900s (Figure 3c, green)		SLD and thickness approximately constant	SLD increases slightly 5.9 × 10 <sup>-6</sup> Å <sup>-2</sup> , and thickness decreases	Layers are relatively stable
8	~1 hr for measurement, Post Cycle 1 (full measurement after 1650 s), Figure 3c, brown		SLD and thickness approximately constant	N/A	Layer 1 remains stable; the SEI layer can no longer be distinguished from the electrolyte, suggesting it has dissolved or that it is porous and has been filled with electrolyte
9	2 <sup>nd</sup> CP (-0.5 mA cm <sup>-2</sup> )	0 < t < 15 s (Figure 4c, blue)	SLD decreases slightly, and thickness increases slightly	N/A	Lithium content of Layer 1 begins to increase
10		15 < t < 30 s (Figure 4c, yellow)	SLD continues to decrease and thickness increases	Thicker layer appears with higher SLD	Evidence of a thick SEI layer atop Layer 1 reappears in the NR pattern
11		30 < t < 45 s (Figure 4c, light green)	SLD continues to decrease and thickness remains approximately constant	Layer becomes more diffuse	Layer 1 continues to increase in content of lithium-containing species, with both layers becoming more diffuse

plating and SEI formation under NRR-relevant current-density cycling conditions, and we note that future cell designs are being developed to optimize N<sub>2</sub> transport and performance under *in situ* NR conditions.

Time-resolved chronopotentiometry and corresponding time-resolved neutron reflectivity data, models, and SLD profiles are presented in Figure 1 and Table 1, Rows 2-5, tracking the time evolution of layer growth at the interface during the application of -0.5 mA cm<sup>-2</sup> to the cathode (see SI, Figure S7, and Table S3 for further

details). We observed an initial decrease in potential toward a plateau between -2.8 and -3 V<sub>Ag/AgCl</sub> at approximately 30 sec, which was then followed by a second decrease in potential to -4.8 V<sub>Ag/AgCl</sub> (Figure 1a). This behavior suggests that there may be two consecutive, distinct processes occurring at the electrode during the two minutes of applied current density. Linear sweep voltammetry (LSV) in this electrochemical cell suggests that Li plating likely occurs near -3 V<sub>Ag/AgCl</sub> (Figure S8), which corresponds to the plateau seen in the chronopotentiometry as well as the standard Li<sup>+</sup>/Li reduction potential. Thus, these two sections of the potential curve may be

related to an initial reordering of electrolyte species such as Li<sup>+</sup> ions and solvent degradation products at the potential plateau, after which the potential becomes increasingly negative as additional reactions of the solvent with the plated Li occur.<sup>34–36</sup>

The time evolution of the SLD profiles of the electrode-electrolyte interface corresponding to the reflectivity models presented in Figure 1b is shown in Figure 1c and represented

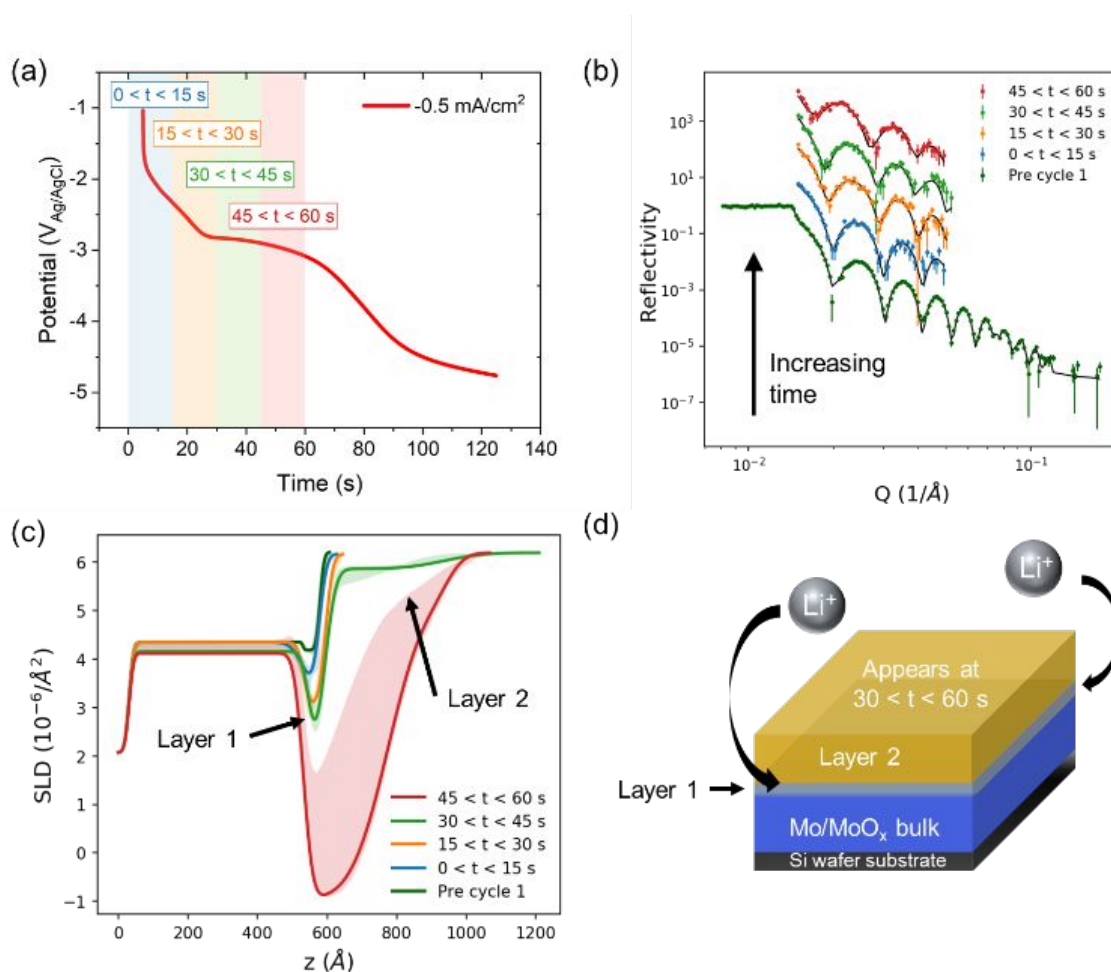


**Figure 1.** (a) Chronopotentiometry at  $-0.5 \text{ mA cm}^{-2}$  for two minutes for a 50-nm Mo film cathode and an electrolyte of  $d_8$ -THF, 0.2 M LiClO<sub>4</sub>, 0.17 M EtOH, pre-sparged with purified N<sub>2</sub>. (b) Reflectivity curves corresponding to the steady-state, pre-chronopotentiometry condition ('Pre cycle 1') and time-resolved reflectivity measurements corresponding to the time points indicated in (a). Reflectivity data were binned in 15-sec intervals, and the time point drop lines in (a) are located at the midpoint of each of these intervals. Reflectivity data in (b) are shown as points. The fit lines in (b) represent the theoretical reflectivity curve of the corresponding modeled interfaces. (c) SLD profiles corresponding to these models for each time interval with the 90% confidence interval as a function of  $z$  for each model shown as a shaded region. For each measurement, the SLD profile corresponds to the best overall model found, which is not necessarily at the center of the confidence level band (see SI). (d) A schematic of layer evolution. In all plotted SLD profiles, the SLD is plotted versus  $z$ , where  $z = 0 \text{ \AA}$  is defined at the surface of the Si wafer, and positive values of  $z$  correspond to the distance from the wafer surface toward the electrolyte.

schematically in Figure 1d. Within the first 30 sec of applying a current density (Table 1, Rows 2 and 3), the SLD of Layer 1 decreases to  $3 \times 10^{-6} \text{ \AA}^{-2}$  while the thickness increases slightly, with the interface between the Mo and the plated layer becoming increasingly rough. We attribute these changes to a possible concomitant increase in Li content within this layer or Li<sup>+</sup> accumulation within the double-layer reduction of the Mo/MoO<sub>x</sub>/MoO<sub>3</sub> surface layer.<sup>29</sup> This reduction of the surface oxide has also been observed via *in situ* GI-XRD (grazing incidence x-ray diffraction) measurements<sup>32</sup> during chronopotentiometry at a higher current density of  $-1 \text{ mA cm}^{-2}$  and

LiClO<sub>4</sub> concentration of 0.5 M, which show the disappearance of the initial MoO<sub>3</sub> peak at  $2\theta = 16.7^\circ$  as charge is passed (Figures S9-S12). Because this surface oxide is likely porous with a low density<sup>37</sup> and the potential of  $-2.3 \text{ V}_{\text{Ag/AgCl}}$  at this timepoint is positive of the Li plating potential (Figure S8), we attribute the decrease in SLD of Layer 1 to Li<sup>+</sup> ions intercalating into the molybdenum oxide as it is reduced as opposed to the appearance of an additional, separate Li-containing layer under these galvanostatic conditions.<sup>38,39</sup> Further below we describe the use of *in-situ* GI-XRD as a means to more deeply characterize the nature of the Li-containing layer, which could

potentially contain a range of Li-based species including (but not limited to)  $\text{Li}_2\text{O}$ ,  $\text{LiOH}$ ,  $\text{Li}_3\text{N}$ , etc.

The continued decrease in the SLD of Layer 1 as the potential reaches the Li plating potential ( $t = 27$  sec and thereafter) is indicative of further accumulation of Li-containing species within this layer, as has been previously reported.<sup>29,38</sup> Although the plateau in potential presented in Figure 1a suggests that Li plating begins to occur at  $t = 27$  s, the modeled SLD values of Layer 1 (Figure 1c) do not reach values that might be associated with a pure Li layer ( $-1 \times 10^{-6} \text{ \AA}^{-2}$ , Table S2) until the binning interval between 45 and 60 sec (Table 1, Row 5). However, it is important to note that because the SLD is calculated via a sum over all atoms in a material and depends on additional factors such as material density, it is difficult to definitively attribute such SLD values to specific compositional species. Lithiation and Li plating are typically identified via neutron reflectometry by a decrease in SLD toward increasingly negative values rather than an SLD value of exactly  $-1 \times 10^{-6} \text{ \AA}^{-2}$ , and the decrease in SLD of Layer 1 presented in Figure 1c is consistent with past neutron reflectometry reports of Li plating in nonaqueous solvents.<sup>25,38,40</sup> Thus, we attribute the decrease in SLD of Layer 1 over the course of these time-resolved measurements to an increase in concentration of lithium-containing species within the layer.

Between  $t = 30$  s and 45 s, the SLD of Layer 1 continued to decrease as the potential decreased to values negative of the Li plating potential (Table 1, Row 4), and the SLD of the layer attributed to the original Mo layer also dropped slightly to about  $4.15 \times 10^{-6} \text{ \AA}^{-2}$ . Although this difference in SLD of about 5% may be a modeling artifact, it could also potentially be attributed to changes in the microstructure of the Mo thin film or Li incorporation, as discussed in the SI. In addition to these observed changes in the "Mo" layer, a second layer (Layer 2) forms on top of Layer 1. Layer 2 appears at a much higher SLD ( $5.9 \times 10^{-6} \text{ \AA}^{-2}$ ) and is significantly thicker and more diffuse than Layer 1, which is consistent with our previous work. The SLD value is slightly lower than that of  $d_8$ -THF ( $6.2 \times 10^{-6} \text{ \AA}^{-2}$ ), which suggests the layer is closely related to  $d_8$ -THF or a related solvent decomposition product, as a lower SLD value would be expected for a product such as  $d_8$ -tetrahydrofuran-2-ol.<sup>41,42</sup> In addition to  $d_8$ -tetrahydrofuran-2-ol, such decomposition products could include species such as 4-hydroxybutanal and 2-ethoxytetrahydrofuran, as both species have been shown to result from either ring-opening reactions of THF with Li metal at the cathode or oxidation of the solvent at the anode in Li-NRR systems.<sup>36,41,43</sup> This layer at the cathode surface might also be expected to include Li ethoxide, which is expected as a by-product of the reaction of  $\text{Li}_3\text{N}$  with EtOH to form  $\text{NH}_3$ . However, Li ethoxide exhibits a very low SLD value ( $-0.143 \times 10^{-6} \text{ \AA}^{-2}$ ), likely precluding its inclusion in Layer 2 in any significant quantity. We therefore refer to Layer 2 as an SEI-type layer, where we define an SEI layer in this system as a layer that does not contain a significant concentration of Li-containing species, and is rather composed of organic electrolyte decomposition products.

The final measurement between  $t = 45$  s and 60 s (Figure 1c, red) shows dramatic differences in SLD profile from the three prior profiles (Table 1, Row 5). The largest changes can be seen in Layer 1 and Layer 2 — Layer 1 exhibits a dramatic decrease in SLD relative to the profile at 30 sec, from approximately  $2.0 \times 10^{-6} \text{ \AA}^{-2}$  to between  $-1$  and  $1 \times 10^{-6} \text{ \AA}^{-2}$ . We note that, by 45 sec, the models become less certain, and such uncertainties allow for a wide range of thickness and SLD values for the SEI (Figure 1c, red shaded region). Thus, the interface between the Li-containing and SEI layers becomes ill-defined as the layers become increasingly diffuse. The potential during this time interval begins to decrease relative to the plateau near the Li-plating potential observed between  $t = 30$  and 45 sec. This decrease in potential is likely related to the observed increase in thickness and diffusivity of both the layers. Indeed, the rapid drop-off in potential after 60 seconds is almost certainly related to the fast buildup of these layers at the surface that resulted in our difficulties modeling the measured reflectivity profiles beyond the first minute of chronopotentiometry (see Figure S7). A value of  $-1 \times 10^{-6} \text{ \AA}^{-2}$  might indicate a layer close to pure metallic Li, while a value of  $+1 \times 10^{-6} \text{ \AA}^{-2}$  could be consistent with a variety of Li-containing species (Table S2). *In situ* GI-XRD measurements during chronopotentiometry at a higher current density of  $-1 \text{ mA cm}^{-2}$  with a higher  $\text{LiClO}_4$  concentration (0.5 M) (Figures S9-S11) suggest that the primary species observed during chronopotentiometry is  $\text{LiOH}$ , which shows a characteristic peak at  $2\theta = 25.63^\circ$  (Figure S12). However, this peak remains small and it is possible that the deposited material that can clearly be observed by eye (Figure S11), is deposited amorphously or has too low of an X-ray scattering cross section to be easily observed with the 17 keV X-rays used. Thus, Layer 1 appears to become significantly enriched with Li-containing species between  $t = 35$  s and  $t = 45$  s, but it is difficult to determine the exact identity of these species.

If Layer 1 were assumed to consist entirely of electrodeposited metallic lithium, with plating beginning at the start of the chronopotentiometry plateau at  $t = 27$  s, then by the end of the potential plateau ( $t = 37$  s), a Li layer with a thickness of 62 Å would be expected to have formed. This thickness would then be expected to increase to 204 Å after 60 sec of chronopotentiometry. The SLD profiles in Figure 1c indicate that Layer 1 is present at potentials positive of the Li plating potential with a thickness between 46 Å and 64 Å (Table S3) and does not increase significantly in thickness until 45 sec  $< t < 60$  sec, at which point the layer grows to 244 Å (Table S3). Thus, because this layer is thicker than would be expected for a pure electrodeposited metallic Li layer and because a layer forms at the Mo surface even before the potential of Li plating is reached, it is likely some portion of the applied current density is being directed toward electrolyte breakdown in addition to plating of metallic Li and possible formation of additional Li-containing species.

Layer 2 additionally grew significantly and decreased in SLD value relative to the previous SLD profile (Figure 1c, green). This growth in thickness could be indicative of a primarily carbonaceous

layer that grows as a result of decomposition of  $d_8$ -THF, while the slight decrease SLD may suggest that this layer also contains Li-containing species that diffuse through the layer to reach Layer 1 and the cathode surface.

*In situ* GI-XRD measurements shed some light upon the possible composition of Layer 1. Figure 2 presents synchrotron GI-XRD that were performed during chronopotentiometry at current

densities  $-1 \text{ mA cm}^{-2}$  for four electrolyte conditions: THF with 0.5 M  $\text{LiClO}_4$  and (1) 0 M EtOH, sparged continuously with  $\text{N}_2$ , (2) 0.17 M EtOH, sparged continuously with  $\text{N}_2$ , (3) 0 M EtOH sparged continuously with Ar, and (4) 0.17 M EtOH sparged continuously with  $\text{N}_2$ . The small pre-chronopotentiometry peak at  $2\theta = 16.7^\circ$  is consistent with a low-intensity  $\text{MoO}_3$  or shifted  $\text{MoO}_2$  peak (Figure

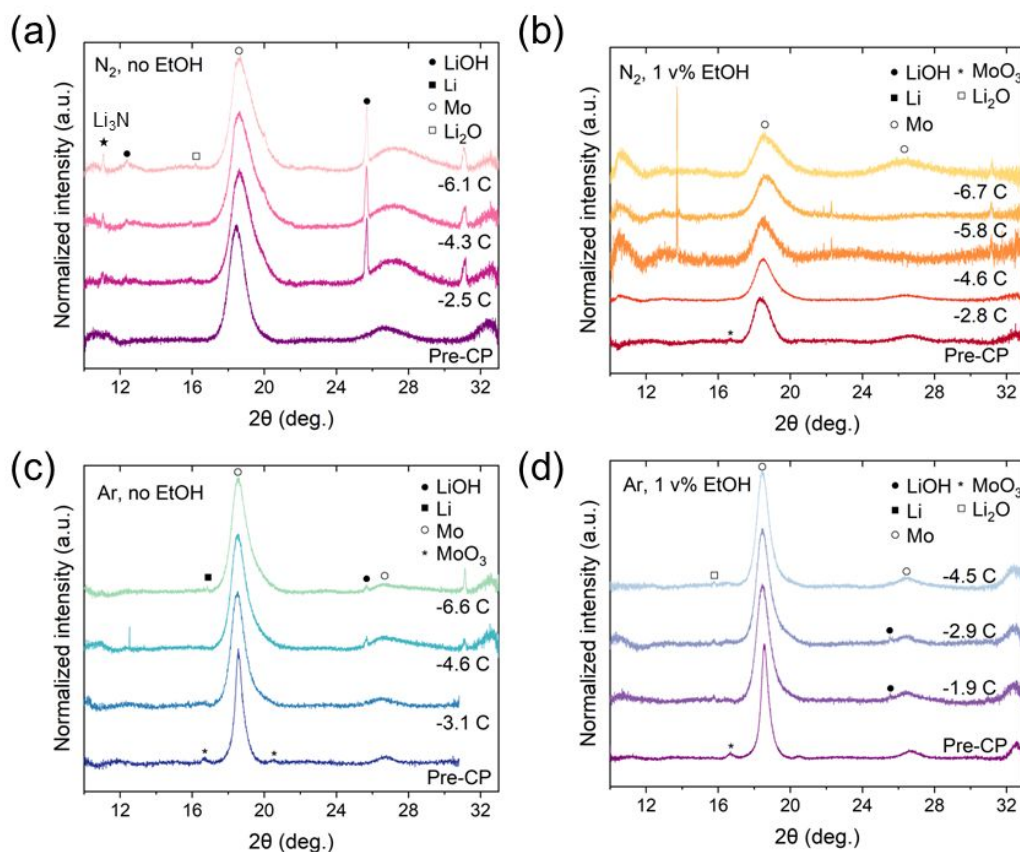


**Figure 2.** Synchrotron GI-XRD measurements of a cathode consisting of 50 nm Mo deposited via PVD onto a Si wafer during chronopotentiometry at  $j = -1 \text{ mA cm}^{-2}$  (see Figure S13) and an X-ray energy of 17 keV ( $0.729 \text{ \AA}$ ). The electrolyte was composed of 0.5 M  $\text{LiClO}_4$  in THF and (a) no EtOH, sparged continuously with purified  $\text{N}_2$ , (b) 0.17 M EtOH, sparged continuously with purified  $\text{N}_2$ , (c) no EtOH, sparged continuously with purified Ar, and (d) 0.17 M EtOH, sparged continuously with purified Ar. Each diffractogram is labeled with the charge passed at the time of the GI-XRD measurement, in coulombs. “CP” refers to “chronopotentiometry.” Pre-CP measurements were made in the electrochemical cell filled with electrolyte before a current density was applied to the cathode. The Inorganic Crystal Structure Database (ICSD) reference patterns used were Mo (52267),  $\text{MoO}_3$  (35076), Li (44367),  $\text{Li}_2\text{O}$  (54368), LiOH (26892), and  $\text{Li}_3\text{N}$  (34280).

S12), the presence of which concurs with pre-electrochemistry XPS measurements of the sample surface, which show the presence of a mixture of  $\text{Mo}^0$ ,  $\text{MoO}_2$ , and  $\text{MoO}_3$  (Figure S14). The two Ar conditions did not reveal XRD peaks in positions that would be consistent with a nitrogen-containing species. Although Figures 2c and 2d might initially appear to show broad peaks between  $2\theta = 10^\circ$  and  $2\theta = 11^\circ$ , closer inspection of the data before background subtraction (Figures S15 and S16) indicate that these peaks arise from the incomplete background subtraction of the data rather than the presence of real peaks. However, other Li-containing species including LiOH,  $\text{Li}^0$ , and  $\text{Li}_2\text{O}$  do appear under Ar conditions, with  $\text{Li}^0$  appearing only without

EtOH. The assignment of the sharp peak at  $31.2^\circ$  remains unclear (see SI for further discussion).

The XRD pattern obtained under  $\text{N}_2$ -saturated, EtOH-excluded electrolyte conditions showed a peak at  $2\theta = 11.1^\circ$ , which we attribute to the  $\alpha$ -phase of  $\text{Li}_3\text{N}$  (Figure 2a, Figure S17). Although this peak is relatively small, it appears clearly relative to the background GI-XRD signal, and its identity is supported by reports in the battery literature that have shown that  $\text{Li}_3\text{N}$  is often observed via XRD by only a single peak near  $2\theta = 11.1^\circ$ ,<sup>44</sup> with the remaining  $\text{Li}_3\text{N}$  peaks being too low in intensity to detect. Given the low observed

peak intensity, we would not expect to observe additional peaks based on the ratio of intensities between the first two peaks shown by the reference  $\text{Li}_3\text{N}$  pattern (Figure S12). Furthermore, when a piece of Li foil was placed in the GI-XRD cell with electrolyte at open-circuit conditions, we again observed the slow appearance of this peak at  $2\theta = 11.1^\circ$  under continuous  $\text{N}_2$  sparging of the pumped electrolyte (Figure S18, S19), suggesting that this peak is indeed related to the presence of  $\text{N}_2$  gas in the presence of  $\text{Li}^0$ .

It additionally appears that the gas environment may affect the extent to which LiOH forms at the electrode surface (Figures 2a and 2c). In general, Li is not reactive in the presence of completely dry gases.<sup>45</sup> It is thus possible that there was simply more trace water in the  $\text{N}_2$ -sparged electrolyte than the Ar-sparged electrolyte, despite our best efforts to minimize water and air exposure by preparing the electrolyte and cell assembly in an Ar glovebox (see SI). However, we note that it has been shown that a film of LiOH present on the surface of Li metal promotes the formation of  $\text{Li}_3\text{N}$ , which can subsequently decompose to LiOH in the presence of water.<sup>45</sup> Thus, the presence of a LiOH film due to the small quantities of water that are likely in this system could promote the formation of  $\text{Li}_3\text{N}$  within the deposited Li layer, thereby promoting the additional formation of LiOH via the decomposition of the nitride.<sup>46,47</sup>

Figure 2b shows that the presumed  $\text{Li}_3\text{N}$  peak does not appear under  $\text{N}_2$  sparging in the presence of 0.17 M EtOH, which are the conditions expected to form  $\text{NH}_3$  at a low  $\text{FE}_{\text{NH}_3}$  (Figure S20). Although a broad peak appeared near  $2\theta = 11^\circ$ , inspection of the XRD patterns before background subtraction (Figure S21) again suggests that this "peak" is simply associated with the baseline fitting and background subtraction rather than the presence of a nitride. However, real peaks do appear at  $2\theta = 13.7^\circ$ ,  $21.8^\circ$ ,  $22.3^\circ$ , and again at  $31.2^\circ$  as was seen for each of the other experimental conditions. Although the peak at  $21.8^\circ$  could be consistent with  $\text{Li}_2\text{O}$  or hydrated LiOH ( $\text{LiOH}(\text{H}_2\text{O})$ ), we cannot definitively attribute this peak to those species because we did not also observe the peaks that would be expected to appear with a higher intensity at lower  $2\theta$  (Figure S12). We do note that the  $\text{Mo}_5\text{Si}_3$  reference pattern shows a peak at  $13.7^\circ$  and has a peak of highest intensity at  $19.2^\circ$  (Figure S22). This could be consistent with the broadening of this Mo peak toward higher  $2\theta$ , although peak broadening has also been attributed to increased microstrain and defect formation in Mo thin films.<sup>48</sup>

Thus, the GI-XRD measurements demonstrated that, for the  $\text{N}_2$ -sparged, EtOH-containing electrolyte used in the neutron reflectometry experiments, Layer 1 would not be expected to contain a large quantity of  $\text{Li}_3\text{N}$ , as crystalline  $\text{Li}_3\text{N}$  was observable via GI-XRD only in an  $\text{N}_2$ -sparged electrolyte without EtOH. For this GI-XRD condition, a long period of time (25 min, -2.5 C passed, Figure 2a) corresponding to deposition of a Li metal layer with a thickness of  $1.76 \mu\text{m}$  on the cathode surface was required in order to observe the  $\text{Li}_3\text{N}$ , which is consistent with past reports that suggest that the formation of  $\text{Li}_3\text{N}$  is the rate-limiting step of the NRR mechanism and the reaction of  $\text{Li}_3\text{N}$  with EtOH is fast.<sup>18</sup> This slow formation may also

be related to the phenomenon that Li nitridation is promoted by impurities such as oxygen and/or water as well as the presence of a LiOH layer.<sup>45,49</sup> Figure 2 also suggests that crystalline Li metal would not be expected to compose a large portion of Layer 1. Rather, it is more likely that Layer 1 consists of a mixture of LiOH,  $\text{LiOH}(\text{H}_2\text{O})$ ,  $\text{Li}_2\text{O}$ , and a small quantity of  $\text{Li}_3\text{N}$  that reacts rapidly with EtOH upon formation. Thus, the increase in content of Li-containing species in Layer 1 shown by the SLD profiles in Figure 1c can likely be attributed to the formation of these species upon quick reaction of plated Li with impurities in the electrolyte rather than the plating of a pure phase of metallic Li.

The presence of a peak at  $2\theta = 31.2^\circ$  in nearly all experimental conditions presented in Figure 2 suggests that either Layer 1 or Layer 2 may contain a crystalline material formed as a result of solvent breakdown that is not dependent on the identity of the sparging gas. This could suggest that the SEI layer may not consist entirely of amorphous species, as might have been expected for a largely carbonaceous SEI.

It is important to consider how the formation of such layered structures at the electrode-electrolyte interface during short cycles of chronopotentiometry may be beneficial or detrimental to the formation of  $\text{NH}_3$  via the NRR mechanism involving formation of  $\text{Li}_3\text{N}$ . Firstly, allowing for the accumulation of  $\text{Li}^+$  ions at the Mo/MoO<sub>x</sub> surface prior to the Li plating potential being reached may facilitate the formation of a thin Li-containing layer, which has been posited to promote  $\text{Li}_3\text{N}$  formation.<sup>16</sup> It may also be possible that this porous SEI layer could promote nitride formation by allowing for better contact time between  $\text{N}_2$  in the electrolyte and Li species present within the pores via the increase in surface area afforded by the porous layer. SEI layers are widely known in the LIB literature to passivate the electrode surface and improve system stability by limiting electrolyte degradation.<sup>50,51</sup> Here, this SEI layer likely controls  $\text{Li}^+$ , EtOH, and  $\text{N}_2$  diffusion to the cathode surface as is evidenced by the lowering of the SLD as the layer grows, which would suggest either that it becomes a solid mixture of species that prevent the electrolyte from contacting the cathode or that Li-containing species may be present within the pores. It is also possible that some portion of this layer is composed of the by-product of the NRR, lithium ethoxide (calculated SLD of  $-0.14 \times 10^{-6} \text{ \AA}^{-2}$ ), which is known to be electronically passivating and could be detrimental to further formation of  $\text{Li}_3\text{N}$  and subsequent conversion to  $\text{NH}_3$ .

Thus, during this first application of a period of current, we observed the development of a bilayer system in which, at potentials just positive of the Li plating potential, there is an accumulation of  $\text{Li}^+$  ions or Li-containing species at the cathode surface that diffuse into the upper Mo/MoO<sub>x</sub>/MoO<sub>3</sub> layer. Upon reaching the Li plating potential, Layer 1 becomes dominated with Li-containing species, on top of which a much thicker, diffuse SEI-type layer (Layer 2) forms. The SLD of this layer begins near that of *d*<sub>8</sub>-THF, suggesting that it is composed of carbonaceous solvent decomposition species, but by 60 sec decreases as the layer increases in thickness, suggesting that the SEI layer either develops a very porous structure or that  $\text{Li}^+$  ions are

diffusing and Li metal is plated within the pores. It is thus clear that the formation of material layers at the electrode-electrolyte interface occurs on a very short timescale, and such layers are highly dynamic even during short periods of chronopotentiometry, almost certainly having large implications on system performance during potential cycling.

### Time-resolved measurements upon return to open-circuit conditions

Immediately following the CP in Figure 1, the cathode was returned to open-circuit conditions (Table 1, Row 6). Using the same time-resolved configuration, neutron reflectivity measurements were performed until the measured open-circuit potential reached a steady-state, which required 48 min (Figure 3a). These time-resolved measurements were initiated 7 min after the cathode had been

returned to open-circuit conditions (see SI, Figure S23 and Table S4 for details). These reflectivity data were binned into 30-sec increments and modeled (Figure S23 and Table S4, see SI discussion for further details), and the time evolution of selected corresponding SLD profiles during this time period are shown in Figure 3c and described in Table 1, rows 6-8. Upon reaching a steady open-circuit potential, a steady-state neutron reflectivity measurement was executed using all seven configurations in order to determine the stable state of the electrode-electrolyte interface (orange curve in Figure S4, and brown curve in Figure 3b, Table S1). We emphasize that these reflectivity measurements performed at OCP were significantly more straightforward to model than those under CP conditions, with the confidence intervals presented in Figure 3c indicating that the slab parameters identified by the DREAM algorithm describe the presented SLD profiles well.

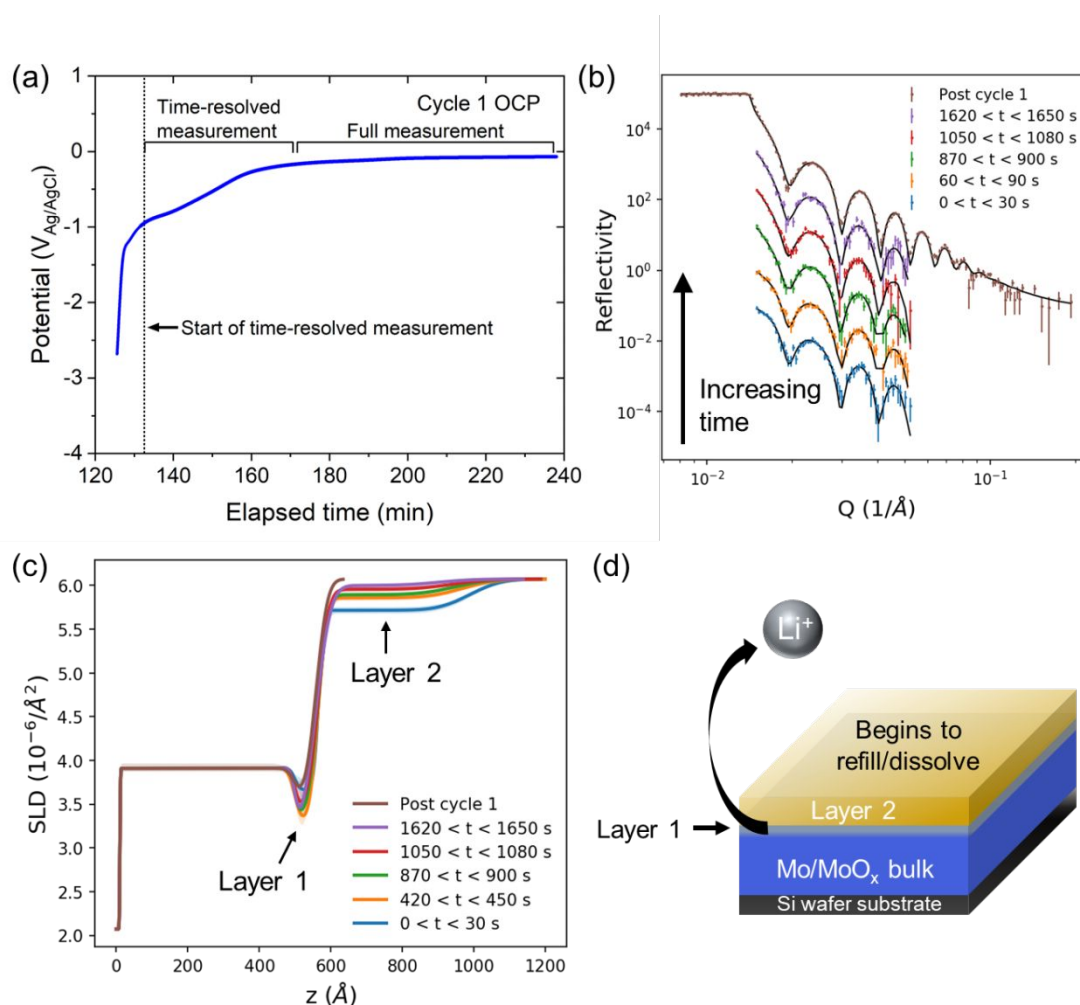


**Figure 3.** (a) Cathode potential versus time at open-circuit conditions. Time periods during which time-resolved and steady-state neutron reflectivity measurements are indicated in brackets. Time evolution of selected (b) reflectivity profiles and (c) SLD profiles obtained from the fits of the neutron reflectivity data during this time period are presented (see Figure S23 and Table S4 for fitted reflectivity data and more detailed model information). Time  $t = 0$  sec in (b) corresponds to the dotted line shown in (a), which occurs 7 min after the start of the return to OCP. The steady-state measurement indicated in (a) (Figure S3, OCP 2) is shown in (b) as "Post cycle 1." A schematic of layer evolution is shown in (d).

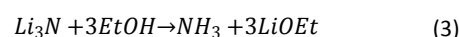
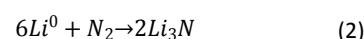
## ARTICLE

Over the course of the time-resolved measurement at OCP, Layer 1 does not vary significantly in SLD and thickness, indicating that this layer is relatively stable at open-circuit conditions. However, we note that the SLD value at the beginning of these time-resolved measurements at OCP ( $3.7 \times 10^{-6} \text{ \AA}^{-2}$ ,  $t = 0$  s in Table S4) is significantly higher than the previously-discussed SLD value reached by Layer 1 during the first period of chronopotentiometry ( $-1 \times 10^{-6} \text{ \AA}^{-2}$ , Table S3, Figure 1c). This higher SLD value is indicative of a significantly lower concentration of Li-containing species in Layer 1 after 7 min at OCP (Table 1, Row 6). It is therefore clear that this layer was highly dynamic during the first 7 min at OCP before time-resolved measurements were initiated, with most of the Li-containing species being removed from the layer. Thus, it appears that Layer 1 stabilized following the removal of the majority of the Li-containing species upon return to OCP.

Contrastingly, Layer 2 exhibited clear changes over the course of these time-resolved measurements at OCP. This layer increased in SLD such that, by the "Post cycle 1" steady-state measurement ("OCP 2" in Figure S4), the layer was no longer distinguishable as a separate layer from the  $d_8$ -THF electrolyte (Figure 3b; Table 1, Rows 7 and 8). The large roughness values of Layer 2 (Table S4) coupled with the increase in SLD value from  $5.7 \times 10^{-6} \text{ \AA}^{-2}$  to  $\sim 6.0 \times 10^{-6} \text{ \AA}^{-2}$ , which is a value close to that of  $d_8$ -THF ( $6.2 \times 10^{-6} \text{ \AA}^{-2}$ ), suggest that the SEI layer may be a porous layer that becomes filled with  $d_8$ -THF. Although the SLD of a porous layer would typically be expected to decrease relative to that of a less-porous layer of that same material, the filling of the pores with a solvent possessing a higher SLD, such as  $d_8$ -THF, would be expected to increase the SLD of the layer. This filling would result in the observed decrease in modeled layer thickness as the contrast in SLD between Layer 2 and the electrolyte steadily decreases. It is possible, then, that the SEI layer either fully dissolves upon reaching a steady-state potential, or that it is highly porous and becomes filled with electrolyte.

Thus, at OCP it appears that a small portion of the Li-containing Layer 1 dissolves either into the SEI layer or into the electrolyte, lowering the concentration of Li-containing species in the layer and leaving behind solvent decomposition species, while the SEI layer fills with electrolyte. We note that, despite the Li content of Layer 1 decreasing, we did not observe a corresponding increase in Li-containing species in the SEI layer (which would be exhibited by a lowering of the SLD), suggesting that the Li-containing species are distributed upward through the SEI layer into the electrolyte at a concentration low enough that they do not significantly influence the SLD of the SEI.

One hypothesis regarding improvements in  $FE_{\text{NH}_3}$  related to current density cycling is that, by returning to open-circuit conditions following the short application of a current density, the plated Li that remains unused in  $\text{NH}_3$  formation is either (1) dissolved from the electrode surface as  $\text{Li}^+$ , recovering plated Li that has not reacted to form the nitride, as well as preventing further decomposition of the THF which results from reaction of the solvent with Li metal, or (2) used to carry out the chemical portion of the reactions in the NRR mechanisms, thus further increasing the  $FE_{\text{NH}_3}$  (Equations 2 and 3 below).<sup>16,52</sup>



Our time-resolved measurements indicate that the Li-containing species within Layer 1 appear to leach out of the layer, suggesting that Li species in the layer may be partially recovered into the electrolyte by returning to open-circuit conditions. However, a stable material layer does remain at the cathode surface, indicating that, as was found in our previous work, returning to OCP does not return the electrode-electrolyte interface to its initial state, and this stable material may be related to carbonaceous electrolyte degradation products containing a lower concentration of Li species.<sup>29</sup> Thus, it appears unlikely that the return to OCP facilitates the uniform deposition of a Li-containing layer during future cycles of chronopotentiometry, as has been posited. An alternative hypothesis consistent with the electrode-electrolyte structure we have observed is that the presence of a rough, thin layer at the electrode-electrolyte interface after the initial cycle may facilitate  $\text{Li}_3\text{N}$  formation by allowing for deposition of Li species onto a material with a high surface area, improving contact of  $\text{N}_2$  with the Li-containing species deposited at the interface.

Additional benefits of returning to open-circuit conditions may be associated with the observed changes in the SEI layer (Layer 2). Returning to OCP appears to allow the SEI layer to refill with and perhaps dissolve in the electrolyte rather than continue to grow, which may facilitate  $\text{Li}^+$  transport through the SEI to Layer 1 and the cathode surface upon subsequent reapplication of current density to the working electrode. Prevention of continued growth of the SEI layer may also minimize the formation of a thicker, more-dense, electronically insulating layer at the cathode surface, which would otherwise pose an obstacle to overall system stability.<sup>16,17,53</sup> Additionally, if Li-containing species were formed/deposited within this porous SEI during chronopotentiometry, the return to OCP may

allow them to redissolve as the pores are filled with electrolyte (indicated by the notable increase in SLD value of Layer 2) while holding them within the network close to the cathode surface. This dissolution would prevent the clogging of these pores with Li-containing species, which could lead to an inability of  $N_2$  to diffuse toward plated Li metal to form  $Li_3N$ . It is thus possible that the benefits associated with current cycling are related to the deposition of a thin layer of Li-containing species within these pores to facilitate contact with  $N_2$  that is dissolved back into the electrolyte upon return to OCP, thereby preventing a loss of Li to build-up within the SEI layer.

#### Time-resolved measurements during second application of current density

Following the return of the cathode to OCP, we again applied a current density of  $-0.5 \text{ mA cm}^{-2}$  for 2 min in a second chronopotentiometry cycle (Figure S24, Table 1, rows 9-11). The time evolution of the reflectivity measurements performed during chronopotentiometry is shown in Figure 4 along with the SLD profiles that correspond to these models (see Table S5 for model parameters). We again observed two regions of increasingly negative cathode potential with plateau behavior in between, although in this second cycle this plateau was not as well-defined and appears at a slightly more positive potential than in the first cycle. A spike in potential appears at 59 sec, which may be related to either bubble

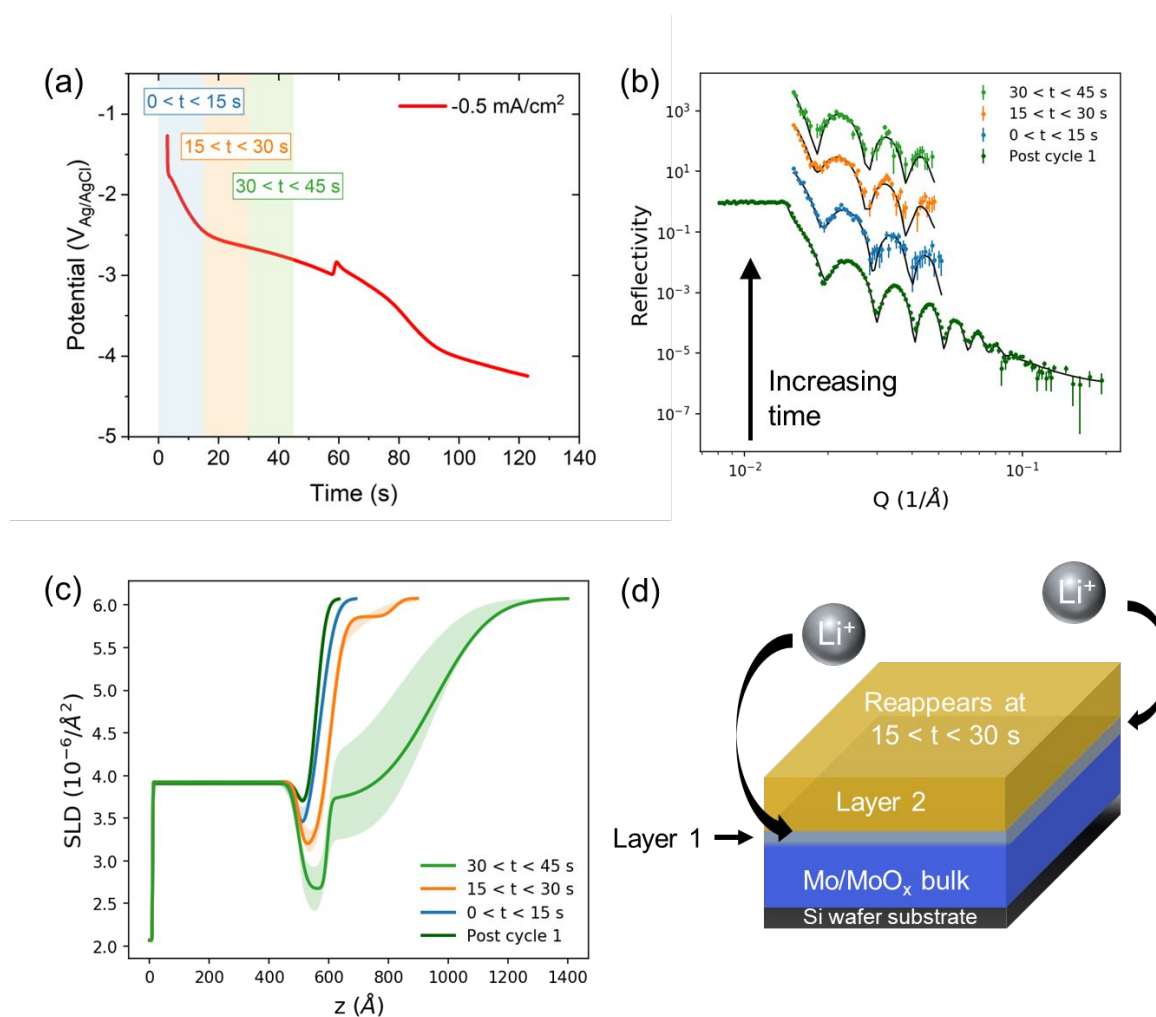


**Figure 4.** (a) Chronopotentiometry at  $-0.5 \text{ mA cm}^{-2}$  for 2 min in the same electrochemical cell. The time points at which the time-resolved neutron reflectivity data were binned are indicated by colored drop lines. The drop lines are located at the midpoint of the binning intervals. Reflectivity curves are shown in (b), with the steady-state reflectivity measurement indicated in Figure 2a presented in dark green as the “Post cycle 1” and the time-resolved reflectivity measurements at 15, 30, and 45 sec shown in the remaining colors corresponding to the time points indicated in (a). Reflectivity data are shown as points, while the modeled reflectivity curves are shown as lines. SLD profiles corresponding to these models at each time point are shown in (c), with the 90% confidence interval as a function of  $z$  for each model shown as a shaded region (see SI for more model details). A schematic of layer evolution is shown in (d).

## ARTICLE

formation at the counter electrode or the initiation of Li plating. Because it is observed between  $-3$  and  $-3.5$   $V_{Ag/AgCl}$  in most of the subsequent cycles (Figure S25), which would be consistent with the point at which Li plating should noticeably occur, this spike may be related to the sudden deposition of Li metal at the surface from the  $Li^+$  ions that have accumulated at the cathode surface and within the SEI pores.

Within the first 15 sec of chronopotentiometry (blue curve), the SLD of Layer 1 immediately begins to decrease and the layer thickness starts to increase, with no second layer present (Table 1, Row 9). This continues throughout the first 30 sec (Figure 4c, yellow; Table 1, Row 10), Li-containing species again become concentrated underneath the electrolyte-filled or dissolved SEI layer.

By 45 sec, Layer 2 again reappears, although it is difficult to comment on the exact SLD values and thicknesses of both layers due

to challenges associated with modeling this reflectivity curve (Table 1, Rows 10 and 11). The confidence interval shown in the shaded region for the green curve indicates that Layer 1 exhibits an SLD value between  $\sim 2.5 \times 10^{-6} \text{ \AA}^{-2}$  and  $3.0 \times 10^{-6} \text{ \AA}^{-2}$  and thickness of the order of  $100 \text{ \AA}$ , while Layer 2 has an SLD that varies between  $\sim 3 \times 10^{-6} \text{ \AA}^{-2}$  and the SLD of the electrolyte, and thickness that appears to extend to about  $400 \text{ \AA}$ . The sudden reappearance of Layer 2 between  $15 < t < 30$  sec and  $30 < t < 45$  sec may suggest that this layer did not fully dissolve at open-circuit conditions. Rather, Layer 2 continued to be present as a porous layer and only became distinguishable from the electrolyte once the application of a current density caused it to become slightly lithiated as  $Li^+$  ions diffused into the pores and started to plate, forming Li-containing species and decreasing the SLD. The sudden reappearance of the layer could have been caused by an increase in the formation of carbonaceous solvent degradation

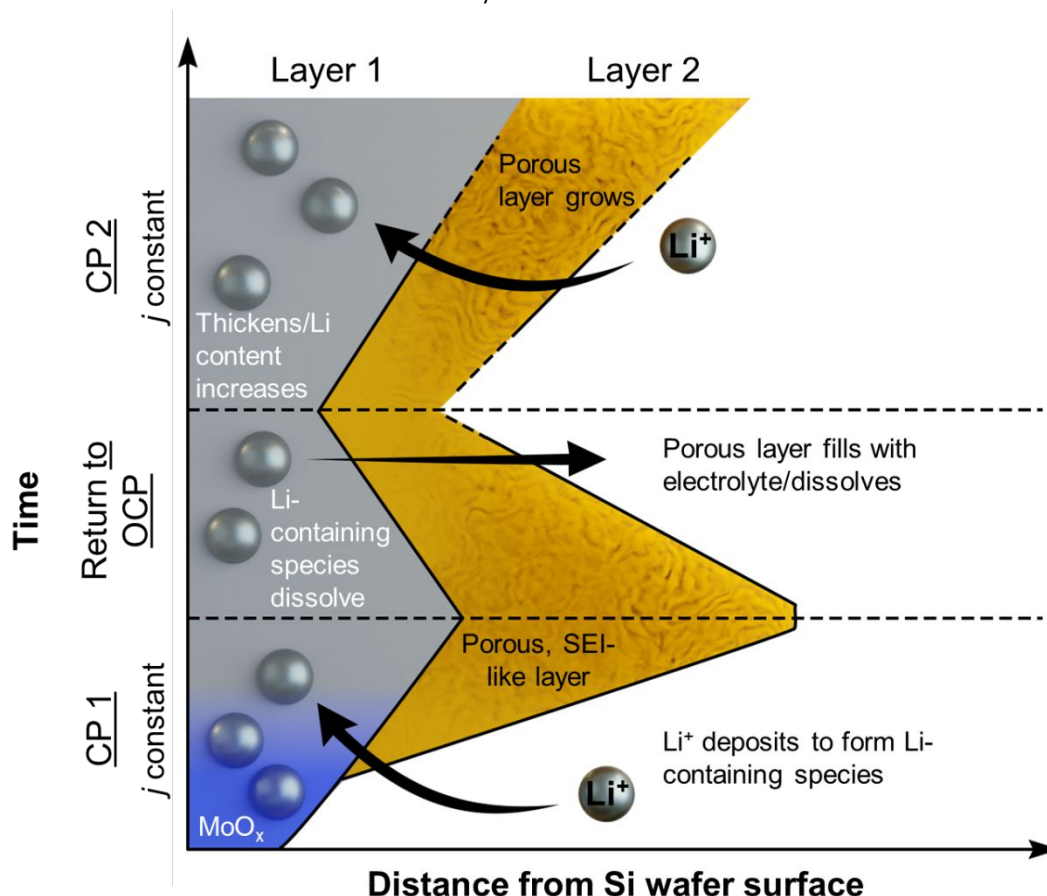


**Figure 5.** Schematic of dynamic electrode-electrolyte interface under cycling-relevant conditions. “CP” refers to “chronopotentiometry,” and “OCP” refers to “open-circuit conditions.”  $j$  refers to applied current density.

## ARTICLE

species within the pores, thereby pushing solvent out of the layer, which would also manifest as a decrease in SLD relative to  $d_8$ -THF, allowing the SEI layer to again become visible in the model. The increase in thickness of Layer 2 in this cycle relative to Cycle 1 may further suggest that, rather than fully dissolving at OCP, some portion of Layer 2 that was too porous to be distinguished from the electrolyte remained stable at the electrode-electrolyte interface. In general, the thickness of the SEI layer appears to increase significantly when the concentration of Li-containing species in Layer 1 noticeably increases.

### Comparison between cycles

The data presented in Figures 1 – 4 provide a broad view of the electrode-electrolyte interface during cycling conditions. During the first application of a current density to the cathode, a layer concentrated in Li-containing species grows within the oxide surface layer as the oxide is reduced, on top of which a thick, diffuse SEI-like layer develops. When the cathode is returned to open-circuit conditions, the lithium content of Layer 1 decreases quickly, leaving a stable, compact layer underneath the SEI-like layer. The porous SEI layer then begins to fill with electrolyte or dissolve to the point that it is no longer distinguishable from the electrolyte after 114 min at OCP. Upon a second application of current density, the compact layer again begins to grow in thickness and increase in Li-containing species content, with the diffuse, SEI-like layer again appearing within the first minute.

Comparing the SLD profiles during Cycle 1 with those modeled during Cycle 2, it appears that the formation of Layer 1 at the electrode-electrolyte interface exhibits similar behavior between the cycles (Figure 5, CP 1 and 2). In general, the composition of Layer 1 at each time point is similar, as is demonstrated by the SLD values of the layer. Layer 2 also exhibits similar behavior between the two cycles, appearing within 30 sec of applied current density in both Cycle 1 and Cycle 2. However, the SLD of Layer 2 drops to lower values more quickly in Cycle 2 than in Cycle 1, which might suggest that Li-containing species may be dispersed within the layer more quickly as Li-containing species are again formed in Layer 1. Such a scenario might be expected if the morphology of the porous SEI network allows for better diffusion of Li-containing species in and out of the SEI layer due to the cycling of the current density (Figure 5).

The presence of this large, diffuse, SEI layer atop the Li-containing layer upon beginning application of subsequent current density cycles likely plays a significant role in the future behavior of the electrode-electrolyte interface. If this porous layer holds Li-containing species closer to the cathode surface when they are

dissolved at OCP and subsequently allows these species to be deposited throughout a carbonaceous network in addition to a concentrated layer (Layer 1) upon subsequent cycles of chronopotentiometry, contact of Li-containing species with  $N_2$  in the electrolyte may be promoted. This could promote  $Li_3N$  formation and subsequent  $NH_3$  formation and thus be related to the improvements in  $FE_{NH_3}$  observed during cycling. In effect, the SEI would be acting as a gas diffusion electrode structure.

Additionally, the thickness of Layer 1 in Cycle 2 was greater than that observed in Cycle 1, suggesting that, with the continuation of cycling, the Li-containing layer atop the electrode would gradually build in thickness. One might assume that, over time, not all the Li-containing species in the layer might dissolve during the OCP portion of cycling, and that the increase in thickness results from the buildup of undissolved Li-containing species over time. However, because the SLD of Layer 1 did not appear significantly different between the two cycles, it is possible that this increase in thickness is instead related to the buildup of insoluble solvent degradation species rather than lack of dissolution of Li-containing species. Thus, these carbonaceous species likely slowly accumulate within the compact Layer 1 over the course of cycling. Given that reports of current density cycling demonstrate that performance can be maintained over many hours,<sup>11,16</sup> rather than inhibiting the formation of  $Li_3N$  by limiting access of  $Li^+$  to the cathode surface, the presence of these degradation species may provide a porous, high surface area onto which Li is deposited, thus providing increased surface area for  $N_2$  to contact the plated Li and form  $Li_3N$ .

Although it is not trivial to extend conclusions based on these measurements toward higher current densities, we anticipate that general trends between applied current density and layer growth will be consistent. Although specific layer parameters such as thickness and porosity likely depend on the current density used, the presence of at least two layers, with one predominantly consisting of Li-containing species and one of solvent degradation species, would be expected. The cathode potential might be expected to decrease more quickly than the potential profiles shown in Figures 1c and 4c with the application of a higher current density due to faster electrolyte degradation resulting in larger overpotentials, but a similar plateau region would likely be expected upon reaching the Li-plating potential. It is more difficult to comment on the extent to which an OCP period affects the “reversibility” of this process and limits SEI formation at higher current densities. Given the reported improvements in performance under current cycling conditions, although the layers observed at the electrode-electrolyte interface may be thicker at higher current densities, OCP still likely at least

partially limits SEI formation by allowing the layer to become more porous and partially dissolve/fill with electrolyte. The exact thickness of the SEI and the Li-concentrated layer underneath would be harder to predict without experimental data. The composition of these layers also may be affected by the applied current density. At higher current densities, it could be possible to observe the formation of other Li-containing species such as  $\text{Li}_2\text{CO}_3$  due to an increase in degradation of the carbonaceous solvent as Li metal is deposited at the electrode surface more quickly.<sup>47,54</sup> Thus, a combination of *in situ* experimental methods would still be required in order to understand the behavior of the system at current densities other than those studied in this work.

Modeling the time-resolved reflectivity measurements executed throughout the remainder of the 6 total chronopotentiometry cycles applied to the cathode (Figure S25) was not possible due to the thickness and roughness of the layers accumulating at the electrode-electrolyte interface. Thus, measurements should also be carried out at a low current density to investigate these interfacial processes more precisely and inform high-current results. Adjustments in cell design to maximize  $\text{N}_2$  transport to the cathode surface would additionally allow for future measurements to be more readily correlated with  $\text{NH}_3$  production. Although the interfacial investigations presented in this work do not allow for precise morphology imaging, such adjustments aimed toward improved system control will enable the design of additional studies of SEI morphology and nanostructure, which should be performed using a combination of complementary characterization techniques.

## Conclusions

This work presents a combined time-resolved *in situ* neutron reflectometry study with insights from *in situ* synchrotron XRD in order to gain insight into the dynamics of the electrode-electrolyte interface and SEI layer under Li-mediated NRR conditions. During two applied-current cycles, a bilayer system forms at the electrode-electrolyte interface in which the layer closest to the electrode is concentrated in Li species, while the larger, more diffuse, porous layer above it is an SEI-like layer likely consisting more of carbonaceous electrolyte degradation products. This Li-containing layer likely contains mixed Li-containing phases, including  $\text{LiOH}$ ,  $\text{Li}_2\text{O}$ , and a small quantity of  $\text{Li}_3\text{N}$  that reacts quickly with  $\text{EtOH}$  upon forming. The return to open-circuit conditions during cycling does not rid the electrode surface of formed material layers; rather, Li-containing species dissolve out of Layer 1, and the porous SEI layer is filled with electrolyte or dissolves. During a second cycle of applied current density, this porous layer appears to either become enriched with Li-containing species or start to fill with solvent degradation species. In the context of improvements in  $\text{FE}_{\text{NH}_3}$  reported for cycling NRR systems, we find that returning the cathode to OCP in between applied current density periods allows for clear recovery of Li species from the electrode-electrolyte interface. It remains unclear whether this return to OCP allows the SEI pores to be filled with electrolyte,

possibly facilitating deposition of Li-containing species throughout the porous network upon subsequent chronopotentiometry, or simply results in complete dissolution of this SEI from the interface, thereby preventing buildup of a passivating, carbonaceous SEI. These measurements reveal the highly dynamic nature of the electrode-electrolyte interface in this system and should be coupled with additional *in situ* methods in order to continue to unravel the complexities associated with the formation of the SEI layer.

## Author Contributions

S.J.B. and M.D. contributed equally to this work in designing the presented experiments and carrying out the subsequent data analysis. For the neutron reflectometry experiments, S.J.B. performed benchtop electrochemical experiments, executed  $\text{H}^1\text{NMR}$  and XPS characterization, and prepared PVD samples. H.W. and C.E.H. assisted with experimental setup at BL 4-B at ORNL. S.J.B. led experiments at BL 4-B with assistance from M.D., A.G., J.E.B., and V.A.N. For the GI-XRD experiments: setup of the electrochemical cell and air-free preparation of the electrochemical cell was conceived of and planned by S.J.B. with mentorship and guidance from A.G. and K.S.; S.J.B. led all synchrotron experiments at SSRL and was assisted by A.G., A.C.N., K.S., P.B., E.J.M., M.E.K., and V.A.N. Benchtop experiments and  $\text{H}^1\text{NMR}$  were performed by S.J.B. with assistance from E.J.M. and P.B. Data analysis was performed by S.J.B. with mentorship from A.G. and K.S.; T.F.J. provided mentorship and guidance for all experiments. All authors contributed to manuscript editing and revision.

## Conflicts of interest

There are no conflicts to declare.

## Acknowledgements

S.J.B. and M.D. contributed equally to this work, and the authors would like to thank Jill Hemman (Oak Ridge National Laboratory) for her help with Figure 5. This work was supported by the Villum Foundation V-SUSTAIN Grant 9455 to the Villum Center for Science of Sustainable Fuels and Chemicals. Sample preparation was supported by the U.S. Department of Energy, Office of Science, Office of Basic Energy Sciences, Chemical Sciences, Geosciences, and Biosciences Division, Catalysis Science Program through the SUNCAT Center for Interface Science and Catalysis. A portion of this research used resources at the SNS, a Department of Energy (DOE) Office of Science User Facility operated by ORNL. Neutron reflectometry measurements were carried out on the Liquids Reflectometer at the SNS, which is sponsored by the Scientific User Facilities Division, Office of Basic Energy Sciences, DOE. ORNL is managed by UT-Battelle LLC for DOE under Contract DE-AC05-00OR22725. XPS characterization of the cathode was performed at the Stanford Nano Shared Facilities (SNSF), supported by the National Science Foundation under award ECCS-2026822. This material is based upon work supported by the National Science Foundation Graduate Research Fellowship under Grant No. DGE-1656518. Any opinion,

findings, and conclusions or recommendations expressed in this material are those of the authors and do not necessarily reflect the views of the National Science Foundation. Use of the Stanford Synchrotron Radiation Lightsource, SLAC National Accelerator Laboratory, is supported by the U.S. Department of Energy, Office of Science, Office of Basic Energy Sciences under Contract No. DE-AC02-76SF00515.

## Notes and references

- (1) Erisman, J. W.; Sutton, M. A.; Galloway, J.; Klimont, Z.; Winiwarter, W. How a Century of Ammonia Synthesis Changed the World. *Nat. Geosci.* **2008**, *1* (10), 636–639. <https://doi.org/10.1038/ngeo325>.
- (2) *World Fertilizer Trends and Outlook to 2022*; Rome, 2019.
- (3) MacFarlane, D. R.; Cherepanov, P. V.; Choi, J.; Suryanto, B. H. R.; Hodgetts, R. Y.; Bakker, J. M.; Ferrero Vallana, F. M.; Simonov, A. N. A Roadmap to the Ammonia Economy. *Joule* **2020**, *4* (6), 1186–1205. <https://doi.org/10.1016/j.joule.2020.04.004>.
- (4) Giddey, S.; Badwal, S. P. S.; Munnings, C.; Dolan, M. Ammonia as a Renewable Energy Transportation Media. *ACS Sustain. Chem. Eng.* **2017**, *5* (11), 10231–10239. <https://doi.org/10.1021/acssuschemeng.7b02219>.
- (5) Chen, J. G.; Crooks, R. M.; Seefeldt, L. C.; Bren, K. L.; Morris Bullock, R.; Darensbourg, M. Y.; Holland, P. L.; Hoffman, B.; Janik, M. J.; Jones, A. K.; Kanatzidis, M. G.; King, P.; Lancaster, K. M.; Lyman, S. V.; Pfomm, P.; Schneider, W. F.; Schrock, R. R. Beyond Fossil Fuel-Driven Nitrogen Transformations. *Science (80-. )*. **2018**, *360* (6391). <https://doi.org/10.1126/science.aar6611>.
- (6) Lan, R.; Irvine, J. T. S.; Tao, S. Ammonia and Related Chemicals as Potential Indirect Hydrogen Storage Materials. *Int. J. Hydrogen Energy* **2012**, *37* (2), 1482–1494. <https://doi.org/10.1016/j.ijhydene.2011.10.004>.
- (7) Tsuneto, A.; Kudo, A.; Sakata, T. Efficient Electrochemical Reduction of N<sub>2</sub> to NH<sub>3</sub> Catalyzed by Lithium. *Chem. Lett.* **1993**, *22* (5), 851–854. <https://doi.org/10.1246/cl.1993.851>.
- (8) Tsuneto, A.; Kudo, A.; Sakata, T. Lithium-Mediated Electrochemical Reduction of High Pressure N<sub>2</sub> to NH<sub>3</sub>. *J. Electroanal. Chem.* **1994**, *367* (1–2), 183–188. [https://doi.org/10.1016/0022-0728\(93\)03025-K](https://doi.org/10.1016/0022-0728(93)03025-K).
- (9) Cai, X.; Fu, C.; Iriawan, H.; Yang, F.; Wu, A.; Luo, L.; Shen, S.; Wei, G.; Shao-Horn, Y.; Zhang, J. Lithium-Mediated Electrochemical Nitrogen Reduction: Mechanistic Insights to Enhance Performance. *iScience* **2021**, *24* (10), 103105. <https://doi.org/10.1016/j.isci.2021.103105>.
- (10) Suryanto, B. H. R.; Matuszek, K.; Choi, J.; Hodgetts, R. Y.; Du, H.; Bakker, J. M.; Kang, C. S. M.; Cherepanov, P. V.; Simonov, A. N.; MacFarlane, D. R. Nitrogen Reduction to Ammonia at High Efficiency and Rates Based on a Phosphonium Proton Shuttle. *Science (80-. )*. **2021**, *372* (6547), 1187–1191. <https://doi.org/10.1126/science.abg2371>.
- (11) Du, H.-L.; Chatti, M.; Hodgetts, R. Y.; Cherepanov, P. V.; Nguyen, C. K.; Matuszek, K.; MacFarlane, D. R.; Simonov, A. N. Electroreduction of Nitrogen at Almost 100% Current-to-Ammonia Efficiency. *Nature* **2022**. <https://doi.org/10.1038/s41586-022-05108-y>.
- (12) Cherepanov, P. V.; Krebsz, M.; Hodgetts, R. Y.; Simonov, A. N.; Macfarlane, D. R. Understanding the Factors Determining the Faradaic Efficiency and Rate of the Lithium Redox-Mediated N<sub>2</sub> Reduction to Ammonia. *J. Phys. Chem. C* **2021**, *125* (21), 11402–11410. <https://doi.org/10.1021/acs.jpcc.1c02494>.
- (13) Suryanto, B. H. R.; Du, H. L.; Wang, D.; Chen, J.; Simonov, A. N.; MacFarlane, D. R. Challenges and Prospects in the Catalysis of Electroreduction of Nitrogen to Ammonia. *Nat. Catal.* **2019**, *2* (4), 290–296. <https://doi.org/10.1038/s41929-019-0252-4>.
- (14) Lazouski, N.; Chung, M.; Williams, K.; Gala, M. L.; Manthiram, K. Non-Aqueous Gas Diffusion Electrodes for Rapid Ammonia Synthesis from Nitrogen and Water-Splitting-Derived Hydrogen. *Nat. Catal.* **2020**, *3* (5), 463–469. <https://doi.org/10.1038/s41929-020-0455-8>.
- (15) Li, K.; Shapel, S. G.; Hochfilzer, D.; Pedersen, J. B.; Krempel, K.; Andersen, S. Z.; Sažinas, R.; Saccoccio, M.; Li, S.; Chakraborty, D.; Kibsgaard, J.; Vesborg, P. C. K.; Nørskov, J. K.; Chorkendorff, I. Increasing Current Density of Li-Mediated Ammonia Synthesis with High Surface Area Copper Electrodes. *ACS Energy Lett.* **2021**, 36–41. <https://doi.org/10.1021/acscenergylett.1c02104>.
- (16) Andersen, S. Z.; Statt, M. J.; Bukas, V. J.; Shapel, S. G.; Pedersen, J. B.; Krempel, K.; Saccoccio, M.; Chakraborty, D.; Kibsgaard, J.; Vesborg, P. C. K.; Nørskov, J.; Chorkendorff, I. Increasing Stability, Efficiency, and Fundamental Understanding of Lithium-Mediated Electrochemical Nitrogen Reduction. *Energy Environ. Sci.* **2020**, *13* (11), 4291–4300. <https://doi.org/10.1039/D0EE02246B>.
- (17) Lazouski, N.; Steinberg, K. J.; Gala, M. L.; Krishnamurthy, D.; Viswanathan, V.; Manthiram, K. Proton Donors Induce a Differential Transport Effect for Selectivity toward Ammonia in Lithium-Mediated Nitrogen Reduction. *ACS Catal.* **2022**, *12* (9), 5197–5208. <https://doi.org/10.1021/acscatal.2c00389>.
- (18) Lazouski, N.; Schiffer, Z. J.; Williams, K.; Manthiram, K. Understanding Continuous Lithium-Mediated Electrochemical Nitrogen Reduction. *Joule* **2019**, *3* (4), 1127–1139. <https://doi.org/10.1016/j.joule.2019.02.003>.
- (19) Cooper, J. M.; Cubitt, R.; Dalgliesh, R. M.; Gadegaard, N.; Glidle, A.; Hillman, A. R.; Mortimer, R. J.; Ryder, K. S.; Smith, E. L. Dynamic in Situ Electrochemical Neutron Reflectivity Measurements. *J. Am. Chem. Soc.* **2004**, *126* (47), 15362–15363. <https://doi.org/10.1021/ja044682s>.
- (20) Ballantyne, A. D.; Barker, R.; Dalgliesh, R. M.; Ferreira, V. C.; Hillman, A. R.; Palin, E. J. R.; Sapstead, R.; Smith, E. L.; Steinke, N.-J.; Ryder, K. S. Electrochemical Deposition of Silver and Copper from a Deep Eutectic Solvent Studied

- Using Time-Resolved Neutron Reflectivity. *J. Electroanal. Chem.* **2018**, *819* (January), 511–523. <https://doi.org/10.1016/j.jelechem.2018.01.032>.
- (21) Koizumi, S.; Ueda, S.; Noda, Y. Time-Resolved Total Reflection Detects Mass Transfer along Thickness Direction of Bulk Nafion® Film. *Phys. B Condens. Matter* **2018**, *551* (December 2017), 163–166. <https://doi.org/10.1016/j.physb.2017.12.029>.
- (22) Schroder, K. W.; Dylla, A. G.; Harris, S. J.; Webb, L. J.; Stevenson, K. J. Role of Surface Oxides in the Formation of Solid–Electrolyte Interphases at Silicon Electrodes for Lithium-Ion Batteries. *ACS Appl. Mater. Interfaces* **2014**, *6* (23), 21510–21524. <https://doi.org/10.1021/am506517j>.
- (23) Veith, G. M.; Doucet, M.; Sacci, R. L.; Vacaliuc, B.; Baldwin, J. K.; Browning, J. F. Determination of the Solid Electrolyte Interphase Structure Grown on a Silicon Electrode Using a Fluoroethylene Carbonate Additive. *Sci. Rep.* **2017**, *7* (1), 1–15. <https://doi.org/10.1038/s41598-017-06555-8>.
- (24) Veith, G. M.; Baggetto, L.; Sacci, R. L.; Unocic, R. R.; Tenhaeff, W. E.; Browning, J. F. Direct Measurement of the Chemical Reactivity of Silicon Electrodes with LiPF<sub>6</sub>-Based Battery Electrolytes. *Chem. Commun.* **2014**, *50* (23), 3081–3084. <https://doi.org/10.1039/c3cc49269a>.
- (25) Fears, T. M.; Doucet, M.; Browning, J. F.; Baldwin, J. K. S.; Winiarz, J. G.; Kaiser, H.; Taub, H.; Sacci, R. L.; Veith, G. M. Evaluating the Solid Electrolyte Interphase Formed on Silicon Electrodes: A Comparison of: Ex Situ X-Ray Photoelectron Spectroscopy and in Situ Neutron Reflectometry. *Phys. Chem. Chem. Phys.* **2016**, *18* (20), 13927–13940. <https://doi.org/10.1039/c6cp00978f>.
- (26) Owejan, J. E.; Owejan, J. P.; DeCaluwe, S. C.; Dura, J. A. Solid Electrolyte Interphase in Li-Ion Batteries: Evolving Structures Measured In Situ by Neutron Reflectometry. *Chem. Mater.* **2012**, *24* (11), 2133–2140. <https://doi.org/10.1021/cm3006887>.
- (27) Jerliu, B.; Do, L.; Hu, E.; Borchardt, G.; Steitz, R.; Geckle, U.; Oberst, V.; Bruns, M.; Schneider, O.; Schmidt, H. Neutron Reflectometry Studies on the Lithiation of Amorphous Silicon Electrodes in Lithium-Ion Batteries. *Phys. Chem. Chem. Phys.* **2013**, *15*, 7777–7784. <https://doi.org/10.1039/c3cp44438d>.
- (28) Jerliu, B.; Steitz, R.; Oberst, V.; Geckle, U.; Bruns, M.; Schmidt, H. Volume Expansion during Lithiation of Amorphous Silicon Thin Film Electrodes Studied by In-Operando Neutron Reflectometry. **2014**. <https://doi.org/10.1021/jp502261t>.
- (29) Blair, S. J.; Doucet, M.; Browning, J. F.; Stone, K.; Wang, H.; Halbert, C.; Avilés Acosta, J.; Zamora Zeledón, J. A.; Nielander, A. C.; Gallo, A.; Jaramillo, T. F. Lithium-Mediated Electrochemical Nitrogen Reduction: Tracking Electrode–Electrolyte Interfaces via Time-Resolved Neutron Reflectometry. *ACS Energy Lett.* **2022**, *7* (6), 1939–1946. <https://doi.org/10.1021/acseenergylett.1c02833>.
- (30) Browning, K. L.; Sacci, R. L.; Doucet, M.; Browning, J. F.; Kim, J. R.; Veith, G. M. The Study of the Binder Poly(Acrylic Acid) and Its Role in Concomitant Solid–Electrolyte Interphase Formation on Si Anodes. *ACS Appl. Mater. Interfaces* **2020**, *12* (8), 10018–10030. <https://doi.org/10.1021/acsami.9b22382>.
- (31) Kienzle, P. A.; O'Donovan, K. V.; Ankner, J. F.; Berk, N. F.; Majkrzak, C. F. REFL1D.
- (32) Blair, S. J.; Nielander, A. C.; Stone, K. H.; Niemann, V.; Kreider, M. E.; Benedek, P.; McShane, E. J.; Avilés Acosta, J.; Gallo, A.; Jaramillo, T. F. Development of a Versatile Electrochemical Cell for in Situ Grazing-Incidence x-Ray Diffraction during Non-Aqueous Electrochemical Nitrogen Reduction. *Manuscr. Prep.* **2022**.
- (33) Saji, V. S.; Lee, C. Molybdenum, Molybdenum Oxides, and Their Electrochemistry. *ChemSusChem* **2012**, *5* (7), 1146–1161. <https://doi.org/10.1002/cssc.201100660>.
- (34) Koch, V. R. Reactions of Tetrahydrofuran and Lithium Hexafluoroarsenate with Lithium. *J. Electrochem. Soc.* **1979**, *126* (2), 181–187. <https://doi.org/10.1149/1.2129002>.
- (35) Aurbach, D.; Daroux, M. L.; Faguy, P. W.; Yeager, E. Identification of Surface Films Formed on Lithium in Dimethoxyethane and Tetrahydrofuran Solutions. *J. Electrochem. Soc.* **1988**, *135* (8), 1863–1871. <https://doi.org/10.1149/1.2096170>.
- (36) Zhuang, G. R.; Wang, K.; Chen, Y.; Ross, P. N. Study of the Reactions of Li with Tetrahydrofuran and Propylene Carbonate by Photoemission Spectroscopy. *J. Vac. Sci. Technol. A Vacuum, Surfaces, Film.* **1998**, *16* (5), 3041–3045. <https://doi.org/10.1116/1.581475>.
- (37) Kent, M. S.; Smith, G. S.; Baker, S. M.; Nyitray, A.; Browning, J.; Moore, G.; Hua, D. W. The Effect of a Silane Coupling Agent on Water Adsorption at a Metal/Polymer Interface Studied by Neutron Reflectivity and Angle-Resolved X-Ray Photoelectron Spectroscopy. *J. Mater. Sci.* **1996**, *31* (4), 927–937. <https://doi.org/10.1007/BF00352892>.
- (38) Avdeev, M. V.; Rulev, A. A.; Bodnarchuk, V. I.; Ushakova, E. E.; Petrenko, V. I.; Gapon, I. V.; Tomchuk, O. V.; Matveev, V. A.; Pleshanov, N. K.; Kataev, E. Y.; Yashina, L. V.; Itkis, D. M. Monitoring of Lithium Plating by Neutron Reflectometry. *Appl. Surf. Sci.* **2017**, *424*, 378–382. <https://doi.org/10.1016/j.apsusc.2017.01.290>.
- (39) Lee, S.-H.; Kim, Y.-H.; Deshpande, R.; Parilla, P. A.; Whitney, E.; Gillaspie, D. T.; Jones, K. M.; Mahan, A. H.; Zhang, S.; Dillon, A. C. Reversible Lithium-Ion Insertion in Molybdenum Oxide Nanoparticles. *Adv. Mater.* **2008**, *20* (19), 3627–3632. <https://doi.org/10.1002/adma.200800999>.
- (40) Veith, G. M.; Doucet, M.; Baldwin, J. K.; Sacci, R. L.; Fears, T. M.; Wang, Y.; Browning, J. F. Direct Determination of Solid-Electrolyte Interphase Thickness and Composition as a Function of State of Charge on a Silicon Anode. *J. Phys. Chem. C* **2015**, *119* (35), 20339–20349. <https://doi.org/10.1021/acs.jpcc.5b06817>.

- (41) Sažinas, R.; Andersen, S. Z.; Li, K.; Saccoccio, M.; Kreml, K.; Pedersen, J. B.; Kibsgaard, J.; Vesborg, P. C. K.; Chakraborty, D.; Chorkendorff, I. Towards Understanding of Electrolyte Degradation in Lithium-Mediated Non-Aqueous Electrochemical Ammonia Synthesis with Gas Chromatography-Mass Spectrometry. *RSC Adv.* **2021**, *11* (50), 31487–31498. <https://doi.org/10.1039/D1RA05963G>.
- (42) Kreml, K.; Pedersen, J. B.; Kibsgaard, J.; Vesborg, P. C. K.; Chorkendorff, I. Electrolyte Acidification from Anode Reactions during Lithium Mediated Ammonia Synthesis. *Electrochem. commun.* **2022**, *134*, 107186. <https://doi.org/10.1016/j.elecom.2021.107186>.
- (43) Du, H.-L.; Matuszek, K.; Hodgetts, R. Y.; Ngoc Dinh, K.; Cherepanov, P. V.; Bakker, J. M.; MacFarlane, D. R.; Simonov, A. N. The Chemistry of Proton Carriers in High-Performance Lithium-Mediated Ammonia Electrosynthesis. *Energy Environ. Sci.* **2023**, *16* (3), 1082–1090. <https://doi.org/10.1039/D2EE03901J>.
- (44) Zhang, Z.; Wu, S.; Yang, C.; Zheng, L.; Xu, D.; Zha, R.; Tang, L.; Cao, K.; Wang, X.; Zhou, Z. Li-N 2 Batteries: A Reversible Energy Storage System? *Angew. Chemie Int. Ed.* **2019**, *58* (49), 17782–17787. <https://doi.org/10.1002/anie.201911338>.
- (45) Markowitz, M. M.; Boryta, D. A. Lithium Metal-Gas Reactions: Interaction of Lithium Metal with Air and Its Component Gases. *J. Chem. Eng. Data* **1962**, *7* (4), 586–591. <https://doi.org/10.1021/je60015a047>.
- (46) Li, K.; Andersen, S. Z.; Statt, M. J.; Saccoccio, M.; Bukas, V. J.; Kreml, K.; Sažinas, R.; Pedersen, J. B.; Shadravan, V.; Zhou, Y.; Chakraborty, D.; Kibsgaard, J.; Vesborg, P. C. K.; Nørskov, J. K.; Chorkendorff, I. Enhancement of Lithium-Mediated Ammonia Synthesis by Addition of Oxygen. *Science (80- )*. **2021**, *374* (6575), 1593–1597. <https://doi.org/10.1126/science.abl4300>.
- (47) Spry, M.; Westhead, O.; Tort, R.; Moss, B.; Katayama, Y.; Titirici, M.-M.; Stephens, I. E. L.; Bagger, A. Water Increases the Faradaic Selectivity of Li-Mediated Nitrogen Reduction. *ACS Energy Lett.* **2023**, *8* (2), 1230–1235. <https://doi.org/10.1021/acseenergylett.2c02792>.
- (48) Rafaja, D.; Köstenbauer, H.; Mühle, U.; Löffler, C.; Schreiber, G.; Kathrein, M.; Winkler, J. Effect of the Deposition Process and Substrate Temperature on the Microstructure Defects and Electrical Conductivity of Molybdenum Thin Films. *Thin Solid Films* **2013**, *528*, 42–48. <https://doi.org/10.1016/j.tsf.2012.06.087>.
- (49) Futamura, N.; Ichikawa, T.; Imanishi, N.; Takeda, Y.; Yamamoto, O. Lithium Nitride Formation on Lithium Metal. *ECS Meet. Abstr.* **2012**, *MA2012-02* (11), 1137–1137. <https://doi.org/0570-0833/88/0808-1101>.
- (50) Zhu, Z.; Chen, X. Artificial Interphase Engineering of Electrode Materials to Improve the Overall Performance of Lithium-Ion Batteries. *Nano Res.* **2017**, *10* (12), 4115–4138. <https://doi.org/10.1007/s12274-017-1647-7>.
- (51) Xu, K. Electrolytes and Interphases in Li-Ion Batteries and Beyond. *Chem. Rev.* **2014**, *114* (23), 11503–11618. <https://doi.org/10.1021/cr500003w>.
- (52) Kreml, K.; Hochfilzer, D.; Cavalca, F.; Saccoccio, M.; Kibsgaard, J.; Vesborg, P. C. K.; Chorkendorff, I. Quantitative Operando Detection of Electro Synthesized Ammonia Using Mass Spectrometry. *ChemElectroChem* **2022**, *9* (6). <https://doi.org/10.1002/celec.202101713>.
- (53) Schwalbe, J. A.; Statt, M. J.; Chosy, C.; Singh, A. R.; Rohr, B. A.; Nielander, A. C.; Andersen, S. Z.; McEnaney, J. M.; Baker, J. G.; Jaramillo, T. F.; Nørskov, J. K.; Cargnello, M. A Combined Theory-Experiment Analysis of the Surface Species in Lithium-Mediated NH<sub>3</sub> Electrosynthesis. *ChemElectroChem* **2020**, 1542–1549. <https://doi.org/10.1002/celec.201902124>.
- (54) Li, S.; Zhou, Y.; Li, K.; Saccoccio, M.; Sažinas, R.; Andersen, S. Z.; Pedersen, J. B.; Fu, X.; Shadravan, V.; Chakraborty, D.; Kibsgaard, J.; Vesborg, P. C. K.; Nørskov, J. K.; Chorkendorff, I. Electrosynthesis of Ammonia with High Selectivity and High Rates via Engineering of the Solid-Electrolyte Interphase. *Joule* **2022**, *6* (9), 2083–2101. <https://doi.org/10.1016/j.joule.2022.07.009>.
- (55) Vrugt, J. A.; ter Braak, C. J. F.; Diks, C. G. H.; Robinson, B. A.; Hyman, J. M.; Higdon, D. Accelerating Markov Chain Monte Carlo Simulation by Differential Evolution with Self-Adaptive Randomized Subspace Sampling. *Int. J. Nonlinear Sci. Numer. Simul.* **2009**, *10* (3), 273–290. <https://doi.org/10.1515/IJNSNS.2009.10.3.273>.
- (56) Nielander, A. C.; Mcenaney, J. M.; Schwalbe, J. A.; Baker, J. G.; Blair, S. J.; Wang, L.; Pelton, G.; Andersen, S. Z.; Enemark-rasmussen, K.; Viktor, C.; Yang, S.; Bent, S. F.; Cargnello, M.; Kibsgaard, J.; Vesborg, P. C. K.; Chorkendor, I.; Jaramillo, T. F. A Versatile Method for Ammonia Detection in a Range of Relevant Electrolytes via Direct Nuclear Magnetic Resonance Techniques. *ACS Catal.* **2019**, *9*, 5797–5802. <https://doi.org/10.1021/acscatal.9b00358>.
- (57) Doucet, M.; Ferraz Leal, R. M.; Hobson, T. C. Web Interface for Reflectivity Fitting. *SoftwareX* **2018**, *7*, 287–293. <https://doi.org/10.1016/j.softx.2018.09.001>.
- (58) Wu, H.-M.; Chen, S.-A. Dopant-Polymer Interaction: MoCl<sub>5</sub>-Doped Polyacetylene. *Synth. Met.* **1988**, *26* (3), 225–236. [https://doi.org/10.1016/0379-6779\(88\)90239-1](https://doi.org/10.1016/0379-6779(88)90239-1).
- (59) McIntyre, N. S.; Johnston, D. D.; Coatsworth, L. L.; Davidson, R. D.; Brown, J. R. X-Ray Photoelectron Spectroscopic Studies of Thin Film Oxides of Cobalt and Molybdenum. *Surf. Interface Anal.* **1990**, *15* (4), 265–272. <https://doi.org/10.1002/sia.740150406>.
- (60) Colton, R. J.; Guzman, A. M.; Rabalais, J. W. Electrochromism in Some Thin-film Transition-metal Oxides Characterized by X-ray Electron Spectroscopy. *J. Appl. Phys.* **1978**, *49* (1), 409–416. <https://doi.org/10.1063/1.324349>.
- (61) Choi, J.-G.; Thompson, L. T. XPS Study of As-Prepared and Reduced Molybdenum Oxides. *Appl. Surf. Sci.* **1996**, *93* (2), 143–149. [https://doi.org/10.1016/0169-4332\(95\)00317-7](https://doi.org/10.1016/0169-4332(95)00317-7).
- (62) Biesinger, M. C. X-ray Photoelectron Spectroscopy (XPS) Reference Pages - Molybdenum

<http://www.xpsfitting.com/2009/10/molybdenum.html>.